Implementation of a Simple Actuator Disc for Large Eddy Simulation ~~(SADLES-V1.0)~~ in the Weather Research and Forecasting Model (~~V4.3.1~~WRF-SADLES-V1.2) for Wind Turbine Wake Simulation

Hai Bui[1,2], Mostafa Bakhoday-Paskyabi[1,2], and Mohammadreza Mohammadpour-Penchah[1,2]

[1]Geophysical Institute, University of Bergen, Allégaten 70, 5007 Bergen, Norway
[2]Bergen Offshore Wind Centre, Allégaten 55, 5007 Bergen, Norway

Correspondence: Hai Bui (hai.bui@uib.no)

Abstract. ~~The development of wind energy in recent years has made the representation of wind turbines in numerical models essential for wind resource and environmental assessment.~~ In this study, we ~~introduce a new wind turbine model, the~~ present the development of a Simple Actuator Disc model for Large Eddy Simulation (SADLES), ~~parameterized in~~ implemented within the Weather Research and Forecast (WRF) model~~. Our goal is to perform~~, which is widely used in atmospheric research. The WRF-SADLES model facilitates both idealized and realistic downscaling of large eddy ~~simulation, so we integrated SADLES and the cell perturbation method as WRF modules and released the code as open-source for further research. We demonstrate the effectiveness of SADLES by comparing a large eddy simulation of a 5-MW wind turbine using the WRF-SADLES~~ simulations, with a focus on resolutions of tens of meters. Through a comparative analysis with the Parallelized Large-eddy ~~simulation~~ Simulation Model (PALM) ~~, showing that SADLES can simulate wind turbine wakes effectively at an intermediate resolution of a few dozen meters . Furthermore, we show the applicability of SADLES in wind farm assessment by downscaling the~~ at resolutions of 10 meters and 30 meters, we validate the effectiveness of WRF-SADLES in simulating the wake characteristics of a 5-MW wind turbine. Results indicate good agreement between WRF-SADLES at 30-meter resolution, 10-meter resolution, and the PALM model. Additionally, we demonstrate a practical case study of WRF-SADLES by downscaling ERA5 reanalysis data ~~to study turbine-to-turbine and farm-to-farm interactions for~~ using a nesting method to simulate turbine wakes at the Alpha Ventus wind farm ~~. In our case study, due to the wind farm to the southwest, the~~ in the South of the North Sea. The meso-to-micro downscaling simulation reveals that the wake effect simulated by WRF-SADLES at the FINO1 offshore meteorological mast station aligns well with the cup anemometer and LiDAR measurements. Furthermore, we investigate an event of farm-to-farm interaction, observing a 16% reduction in ambient wind speed ~~at Alpha Ventus is reduced by 14% and the~~ and a 38% decrease in average turbine power ~~is reduced by 35%. SADLES provides~~ at Alpha Ventus due to the presence of a wind farm to the southwest. WRF-SADLES offers a promising balance between computational efficiency and accuracy for wind turbine wake simulations~~and has potential applications in wind energy assessment~~, making it valuable for wind energy assessments and wind farm ~~construction~~ planning.

1   Introduction

Wind energy has become increasingly important due to the pressing need to address climate change and reduce our reliance on fossil fuels. It is crucial to have a deep understanding of the complex interaction between wind turbines and the atmospheric boundary layer (ABL) for effective wind energy assessment and wind farm construction planning. In particular, the wake created behind upstream turbines can have a significant impact on the performance of downstream turbines, resulting in reduced power production, increased turbulence, and dynamic loading (Porté-Agel et al., 2020; Bakhoday-Paskyabi et al., 2022a). Large eddy simulation (LES) is a powerful tool that can simulate ABL turbulence with high spatial and temporal resolution, making it an invaluable resource for studying turbine wakes and and their interaction with the ABL (Breton et al., 2017).

To model the turbine wakes, various methods can be used to simulate the rotor with varying levels of accuracy and computational cost. The most accurate, but computationally expensive methods are the actuator surface (AS) and actuator line (AL) models, which typically use the ~~blade element method (BEM, Burton et al., 2011; Göçmen et al., 2016)~~ Blade Element Momentum (BEM) theory or the Blade Element Theory (BET) (Burton et al., 2011; Göçmen et al., 2016) to calculate the thrust and torque acting on the turbine blades. A less computationally expensive method is the actuator disc with rotation (AD+R) model, where the turbine blades are represented by a rotating circular disc that extracts energy from the wind through axial and azimuthal forces. The actuator disc without rotation (AD) is the simplest form, where only the axial force is considered. These methods have been applied in various LES models, such as the EllipSys3D model (Göçmen et al., 2016, AL), the MITRAS model (Salim et al., 2018, AD+R), the Simulator for Wind Farm Applications (SOWFA) (Fleming et al., 2014; Churchfield et al., 2016, AL), and the Parallelized Large-eddy simulation Model (PALM) (Witha et al., 2014; Maronga et al., 2015, 2020, AL, AD, AD+R). For applications that do not require a very high resolution and detailed near wake structures, the AD+R and AD methods are often favorable as they require fewer computational resources, are easier to implement, and yet achieve an adequate level of accuracy for far wake information (Breton et al., 2017)

Besides the accuracy of the turbine wake methods, a realistic ABL plays a crucial role in wake simulations. The processes that affect wind farms range from macro- and ~~meso-scale~~ mesoscale weather phenomena, such as cyclones and fronts, down to the micro-scale of turbulence in the ABL (Porté-Agel et al., 2020). Given this multi-scale nature, a ~~macro-to-micro~~ meso-to-micro numerical downscaling could be useful in simulating the ABL-turbine interaction realistically and understanding its underlying mechanisms (Muñoz-Esparza et al., 2014; Bakhoday-Paskyabi et al., 2022a). To incorporate realistic ABL conditions, one can use the meso-micro offline coupling approach, i.e. the output of a mesoscale model is used as the driven boundary condition for the dedicated LES models (e.g. Wang et al., 2020; Lin et al., 2021; Bakhoday-Paskyabi et al., 2022b; Onel and Tuncer, 2023). However, this approach depends on the frequency of the mesoscale model output, which is often not enough for ~~short time~~ short-time scale processes. The second approach, online coupling, ~~is using~~ uses a meso-micro coupled model system, where a mesoscale model and ~~a LES model~~ an LES model are coupled through a coupling interface. While the online coupling approach provides a seamless downscaling, it is more difficult to implement than the offline approach. The third approach, nested downscaling, is using a single model that can handle the downscaling naturally through a system of nested domains where the ~~outer and~~ inner domains can be configured to run in LES mode. For example, the Consortium for Small-scale

Modeling (COSMO) model (Baldauf et al., 2011) and the Weather Research and Forecast (WRF) model (Skamarock et al., 2019) provide this capability.

The ~~purpose of this study is to develop a macro-to-micro nested downscaling framework that can simulate turbine wakes~~ ~~with realistic ABL conditions. We chose the WRF model as it is an~~ WRF model is open-source ~~model widely used by the research community to study~~ software that is highly popular in the atmospheric research community for studying a wide range of atmospheric processes, from idealized studies to real-world applications. It facilitates a meso-to-micro nested downscaling framework capable of simulating turbine wakes under realistic Atmospheric Boundary Layer (ABL) conditions (Muñoz-Esparza et al., 2014; Bakhoday-Paskyabi et al., 2022a; Ning et al., 2023). There are several WRF implementations that include the effects of wind farms and wind turbines ~~(e.g. Fitch et al., 2012; Volker et al., 2015; Mirocha et al., 2014; Kale et al., 2022)~~ (e.g., Fitch et al., 2012; Volker et al., 2015; Mirocha et al., 2014; Kale et al., 2022), which can be grouped into wind farm parameterization (WFP) and wind turbine model (WTM).

The WFP approaches (Fitch et al., 2012; Volker et al., 2015) are commonly used to study the collective effects of wind turbine wakes on the ABL and the interactions between wind farms (e.g. Pryor et al., 2020; Fischereit et al., 2022). One advantage of these approaches is their low computational cost and ease of implementation. For example, (Fitch et al., 2012) only requires the thrust and power curve data from turbine manufacturers. However, due to the limitation of the target horizontal resolutions, which must be at least 3 to 5 rotor diameters (Fischereit et al., 2022), the WFP cannot explicitly resolve individual turbine wakes ~~explicitly, nor~~ or turbine-to-turbine interactions. This may result in inaccurate evaluations of wakes behind wind farms (Lee and Lundquist, 2017).

~~the implemented general actuator disc (GAD) model (Mirocha et al., 2014; Kale et al., 2022) in WRF uses the AD+R method that is based on the BEM theory. However, the GAD requires high resolution, with at least a few grid points across the rotor disc (Mirocha et al., 2014), making the simulation costly for large arrays of turbines or multiple wind farms. Compared to the WFP approaches, the GAD model requires more information about the turbine, such as blade profiles and aerodynamic characteristics, as well as generator speed and blade pitch control. This information is sometimes confidential and not publically available. Finally, despite the open-source availability of the WRF, the source code for the GAD implementation has not been publicly released, limiting its use for the scientific community.~~

On the other hand, the implemented general actuator disc (GAD) model in WRF (Mirocha et al., 2014; Kale et al., 2022) employs the AD+R method based on the BEM theory. However, due to the requirement for high resolution, with at least a few grid points across the rotor disc, the simulation can become costly for large arrays of turbines or multiple wind farms. Additionally, the GAD model requires more information about the turbine, such as blade profiles and aerodynamic characteristics as well as generator speed and blade pitch control, which may sometimes be confidential and not publicly available. Finally, the GAD implementation's source code has not been released publicly, limiting its use for the scientific community, despite the WRF being open-source.

In this study, we developed a new wind turbine parameterization (WTP) model ~~,~~ named the Simple Actuator Disc for Large Eddy Simulation (SADLES)~~, which is a compromise~~. SADLES bridges the gap between the Generalized Actuator Disc (GAD) and Wind Farm Parameterization (WFP) models within the Weather Research and Forecasting (WRF) model. ~~The purpose of~~

~~this model is to simulate the turbine wake explicitly for intermediate resolutions between the GAD and WFP models, e.g.~~ It simulates turbine wakes explicitly at intermediate resolutions (e.g., tens of meters~~. SADLES uses the AD~~) between those achievable with GAD and WFP. Similar to the WFP model proposed by Fitch et al. (2012), SADLES employs the actuator disc (AD) method and requires only basic information about the turbines, such as their thrust and power curves~~, similar to the WFP model proposed by Fitch et al. (2012)~~. To accommodate the ~~Large Eddy Simulation (LES)~~ LES downscaling approach, we also implemented the cell perturbation method (Muñoz-Esparza et al., 2014), which is necessary for generating turbulence in the nested domains. ~~We integrated SADLES~~ The WRF-SADLES code package is an open-source software suite that includes both the SADLES module and the cell perturbation ~~method as WRF modules and released the code as open-source with the aim of including the model in the~~ module. Its development aims for integration into the official WRF repository~~for~~, thereby promoting further open research within the weather forecasting community.

To validate the WRF-SADLES model, we chose to compare its idealized simulations of a 5-MW wind turbine with similar simulations using the PALM model. The reason for selecting PALM was that it includes a wind turbine model ~~(PALM-WTM)~~ that uses the AD+R method, which is comparable with the AD method used by the WRF-SADLES, but with higher accuracy. Moreover, the ~~PALM-WTM~~ PALM model has been shown to agree well with more sophisticated wake models and observations (Witha et al., 2014; Vollmer et al., 2015; Bakhoday-Paskyabi et al., 2022a, b). In addition, we demonstrated a more realistic application of the WRF-SADLES by downscaling the ERA5 reanalysis data (Hersbach et al., 2020) to a ~~40-m~~ 40-meter resolution around the Alpha Ventus wind parks, enabling us to investigate the effects of turbine-to-turbine and farm-to-farm interactions. The simulations are then compared with the observational data recorded at the FINO1 offshore meteorological mast station.

The rest of the paper is organized as follows~~.~~: Section 2 describes the ~~implementation of the SADLES model~~ the method and implementation of WRF-SADLES. Section 3 ~~describes~~ presents an idealized simulation with a single 5-MW wind turbine and compares it with the PALM model. Section 4 ~~provides~~ offers an example application of a multi-scale ~~down-scaling application~~ downscaling approach with multiple wind farm simulations. Finally, Section 5 discusses the potential applications and limitations of the SADLES model.

2 Methods

2.1 The simple actuator disc for large eddy simuation

The actuator disc (Anderson, 2020) is a hypothetical surface perpendicular to the wind flow that extracts energy continuously from the ambient wind through the work of the thrust force:

$$\mathbf{F}_T = -\frac{1}{2}\rho C_T |\mathbf{V_0}|\mathbf{V_0}A, \qquad (1)$$

where ρ is the air density, A is the rotor area, C_T is the thrust coefficient, which is a function of the ambient (unperturbed) wind speed $|\mathbf{V_0}| = \sqrt{u_0^2 + v_0^2}$. The wind speed at the rotor, $\mathbf{V}$, is reduced by the axial induction factor a through the relation:

$$\mathbf{V} = \mathbf{V_0}(1-a). \qquad (2)$$

The tendency terms of the thrust force are incorporated into the WRF model at the grid cells where the actuator disc intersects:

$$\left.\frac{\partial u}{\partial t}\right|_T = -\frac{1}{2}C_T|\mathbf{V_0}|u_0\frac{\delta A}{\Delta x \Delta y \Delta z}, \tag{3}$$

$$\left.\frac{\partial v}{\partial t}\right|_T = -\frac{1}{2}C_T|\mathbf{V_0}|v_0\frac{\delta A}{\Delta x \Delta y \Delta z}, \tag{4}$$

~~Where~~ where δA is the portion of the actuator disc area within the grid cell, Δx, Δy, and Δz are the grid sizes. We can shorten the formula by defining the area factor $F_A = \delta A/(\Delta x \Delta y \Delta z)$, which can be determined by performing a vertical and horizontal discretization of the actuator disc area (Fig. 1).
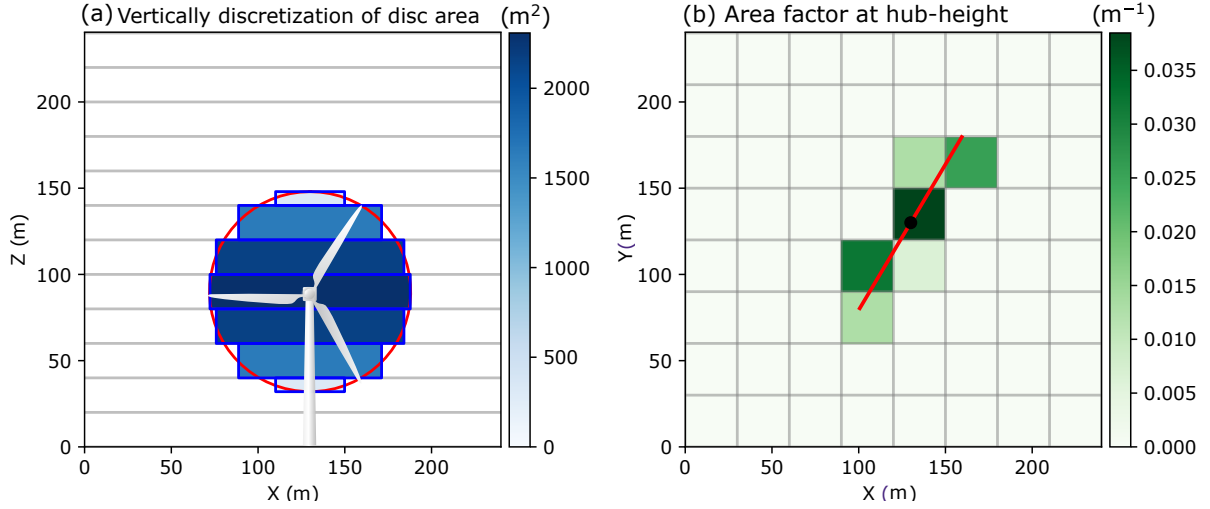
Figure 1. ~~An example of vertical~~ The illustration demonstrates the discretization of an actuator disc. (a) ~~and horizontal discretization~~ Vertically, the disc is divided into sections between each full vertical level. (b) ~~of an actuator disc~~ The discretized area factor at the hub-height level is depicted. The ~~turbine~~ actuation disc radius is ~~58 m~~ 116 meters, and ~~the grid size is 30 m for~~ both horizontal and vertical ~~grids~~ grid sizes are 30 meters for illustrative purposes.

We note that in the WRF model, the tendency terms are defined for the coupled velocity, which is defined as $U = \mu_d u$, with μ_d ~~is~~ as the dry mass of ~~the~~ air column. It is also more convenient to use the wind speed at the rotor disc instead of the ambient wind speed. Thus the tendency terms to be added to the model become:

$$\left.\frac{\partial U}{\partial t}\right|_T = -\frac{1}{2(1-a)^2}\mu_d C_T|\mathbf{V}|u F_A \tag{5}$$

$$\left.\frac{\partial V}{\partial t}\right|_T = -\frac{1}{2(1-a)^2}\mu_d C_T|\mathbf{V}|v F_A \tag{6}$$

In ~~contrast to the GAD model,~~ the ~~simple AD model does not explicitly represent the rotational effect. Instead, the rotational effect is treated as the~~ wind farm parameterization proposed by Fitch et al. (2012), turbulent kinetic energy (TKE) is introduced in proportion to the difference between the thrust coefficient and the power coefficient ($C_T - C_P$). This addition is justified by the extraction of kinetic energy from the mean flow, where part contributes to power production, and the remainder is transferred to TKE. The question arises: is this approach valid or necessary for the micro-scale actuator disc model? For instance, the exclusion of rotational effects can be viewed as subgrid-scale turbulence ~~that affects the~~ impacting wake recovery. ~~This effect is represented by adding~~ To investigate, we adopt the method used by Fitch et al. (2012), incorporating a source of subgrid-scale ~~turbulent kinetic energy (TKE), similar to the approach used in Fitch et al. (2012)~~TKE as:

$$\frac{\partial \mathrm{TKE}}{\partial t} \frac{\partial TKE_{sgs}}{\partial t}\bigg|_T = \frac{1}{2(1-a)^3}\mu_d C_{TKE}|\mathbf{V}|^3 F_A \tag{7}$$

where $C_{TKE} = f_{TKE}(C_T - C_P)$, C_P is the power coefficient, and f_{TKE} is a factor that controls the amount of kinetic energy loss is converted to TKE.

The tendency terms above depend critically on the axial induction factor a. Some previous studies have used certain specific values of a, such as $a = 1/4$ (Calaf et al., 2010) or even $a = 0$ (Fitch et al., 2012) (i.e. they used the wind speed at the grid point directly instead of the unperturbed wind speed). In our implemented SADLES model, we provide two options for estimating a:

- Option 1 (direct evaluation): First, the hub-height ambient wind speed $|\mathbf{V}_0|$ is evaluated at two rotor diameters ($2D$) in front of the turbine. Then, the induction factor is calculated by:

  $a = 1 - \frac{|\mathbf{V}|}{|\mathbf{V_0}|}$,

  ~~where $\mathbf{V}$ is the wind speed at the rotor location.~~

- Option 2 (inferred evaluation): In this option, only the hub-height wind speed at the rotor location is needed. Instead, we assume the 1-dimensional momentum theory ($C_T = 4a(1-a)$) and therefore:

  ~~$a = \frac{1}{2}(1 - \sqrt{1 - C_T(|\mathbf{V}|)})$~~ $a = \frac{1}{2}(1 - \sqrt{1 - C_T(|\mathbf{V}|)})$.

  Note that although the thrust curve is typically provided as a relation between C_T and the ambient wind speed $|\mathbf{V}_0|$, we can also establish the relation between C_T and the wind speed at the rotor $|\mathbf{V}|$ using the 1-dimensional momentum theory.

In general, the direct evaluation of a (Option 1) ~~should be more accurate~~is more intuitive. However, this method has some potential problems, including the formula being affected by the blockage effect, where the wind speed in front of the wind turbine is reduced. By using this formula, a can exceed 0.5, ~~which is nonphysical because it assumes~~implying that the wind behind the turbine becomes opposite to the ambient wind. This is nonphysical and can lead to model instability~~in some situations~~. Thus, the upper limit of a is set to the inferred evaluations of a (Option 2). ~~In cases where the resolution is coarse, for example,~~

2.2 Cell perturbation

Traditional LES simulations often use periodic lateral boundary conditions, which allow turbulent eddies to fully develop into a pseudo-equilibrium state. However, in our LES downscaling approach, the limited time and space available at the inflow boundary can prevent eddies from fully developing, particularly in cases with a small inner domain, high ambient wind speed, or stable boundary layer conditions. This can lead to incomplete development of the eddies and potentially affect the accuracy of the simulation.

The above problem can be alleviated using the cell perturbation method (Muñoz-Esparza et al., 2014, 2015), which is a simple and effective way to improve the realism of turbulent representations. The method adds a random perturbation of potential temperature within the interval [–0.5, 0.5] to three cells of $8{\times}8$ grid points near the chosen boundaries. In the idealized setup of Muñoz-Esparza et al. (2014), perturbations are introduced at every vertical grid point up to two-thirds of the inversion layer, which is known in the idealized setting. In our approach, the perturbations are applied with full magnitude up to a pre-defined vertical level k_1 and then gradually reduced to zero at a higher level k_2 using the weight $\cos^2\left[0.5\pi(k-k_1)/(k_2-k_1)\right]$, where k is the vertical level. As noted by Muñoz-Esparza et al. (2014), the perturbation process should not be done at every time step, but at an interval that is at least equal to the perturbation time scale, $T_s = 8\Delta x/U$, where U is the characteristic velocity scale and Δx is the horizontal grid spacing.

Because the cell perturbation method is not available with the distribution of WRF, we included our implementation within the distribution of ~~SADLES~~WRF-SADLES.

2.3 Code implementation and turbine information

We~~have incorporated~~'ve integrated the SADLES code into the Advanced Research WRF (ARW), ~~version4.3~~version 4.3.1, with MPI support. This was achieved by adding two new Fortran 90 modules: a SADLES module (~~module_sadles.F~~*module_sadles.F*) and a cell perturbation module (~~module_cellpert.F). To use the code, users can copy these modules and override few related files to the existing WRF file structure and recompile the model system. Table A1 and Table A2 provide information on the options available~~ *module_cellpert.F*), both serves as the WRF's physics package (located in the *phys* directory). The new namelist options for these modules were incorporated into the WRF model by modifying the WRF's Registry. During the first step of the Runge-Kutte loop (within *module_first_rk_step_part1.F*), tendency terms of the SADLES module are added to the model, while the potential temperature perturbation from the cell perturbation is incorporated after the integration loop (within *solve_em.F*).

Tables A1 and A2 outline the available options in the SADLES and cell perturbation modules. ~~The~~ This modified WRF system ~~can also be used to simulate~~ also enables the simulation of turbine behavior in idealized experiments~~by~~, with additional namelist options ~~to specify~~ for specifying the Coriolis parameter and surface roughness length. The code has been ~~made available~~ released as open-source to ~~promote open research and we hope it will be included~~ foster open research (Bui, 2023)

Table 1. Domain configurations for the idealized WRF (prefix W) and PALM (prefix P) experiments

Experiments	Domain	$N_x \times N_y \times N_z$	$\Delta x[m]$	Δt [s]	L_x [m]	L_y [m]
W30m_Opt1, W30m_Opt2,	D01	$322 \times 163 \times 91$	90	1/2	28890	14490
	D02	$322 \times 163 \times 91$	30	1/6	9660	4860
W30m_TKE0, W30m_TKE1						
W10m_Opt1, W10m_Opt2,	D01	$322 \times 163 \times 91$	30	3/20	9660	4860
	D02	$448 \times 163 \times 91$	10	1/20	4470	1620
W10m_TKE0, W10m_TKE1						
P30m	D01	$336 \times 172 \times 90$	90	1/2	30240	15480
	D02	$336 \times 192 \times 160$	30	1/6	10080	5760
P10m	D01	$336 \times 176 \times 160$	30	3/20	10080	5280
	D02	$432 \times 192 \times 150$	10	1/20	4320	1920

, with the aspiration of its inclusion in the official WRF repository~~in the future~~. Users can implement the WRF-SADLES by copying these modules and overriding a few related files within the existing WRF file structure, followed by recompiling the model system. In the ~~next~~ subsequent section, we ~~use the turbine information~~ utilize turbine data from Larsén and Fischereit (2021), which ~~contains~~ provides the locations, thrust curves, and ~~powers~~ power curves of wind turbines ~~of several~~ from various wind farms in the North Sea.

3 ~~Example 1:~~ Idealized simulation

3.1 ~~Expriment~~ Experiment design

To start, we investigate the calculation of the axial induction factor (e.g., Option 1 or Option 2) and the additional tendency for sub-grid TKE (i.e., f_{TKE}). Due to challenges in acquiring relevant observational data, we conducted and compared idealized experiments ~~involving~~ employing a single 5-MW turbine using the WRF-SADLES and ~~the PALM models. The simulations are performed at two resolution of~~ PALM models, known for their realistic simulation of turbine wakes. Simulations were executed at two resolutions: 10 ~~m~~ meters (high resolution) and 30 ~~m~~ meters (target intermediate resolution).

Table 1 summarizes the experiments conducted using the WRF-SADLES and PALM models. For the WRF-SADLES simulations, experiments with suffixes _Opt1 and _Opt2 represent different options for calculating the axial induction factor a, with Option 1 employing direct evaluation and Option 2 employing inferred evaluation. In these experiments, f_{TKE} takes the default value of 0.5. Additionally, experiments with suffixes _TK0 and _TKE1, both utilizing Option 2, aim to investigate the effect of adding TKE tendency as in Equation (7), with f_{TKE} set to 0 and 1, respectively.

~~WRF~~ WRF-SADLES configurations

~~In this example, we performed four idealized experiments using WRF-SADLES included two different resolutions (10 m and 30 m) and two different options for evaluating the axial induction factor (SADLES Opt1 and Opt2, representing direct and inferred evaluations, respectively).~~
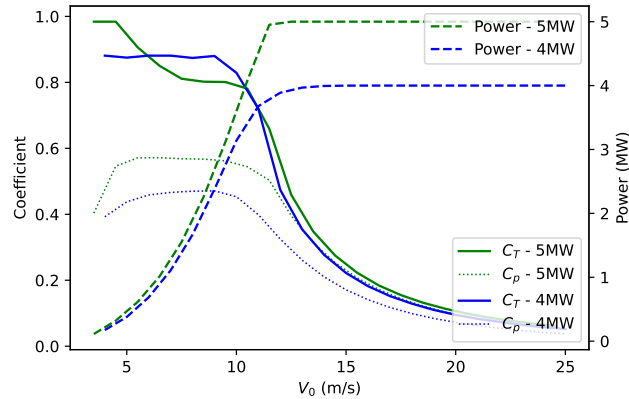
Figure 2. Thrust coefficient (C_T), power coefficient (C_P), and turbine power as functions of ambient wind speed (V_0) are shown for the 4 MW and 5 MW wind turbines used in the idealized (5 MW) and realistic (4 MW and 5 MW) experiments in this paper.

220   The domain configurations for each experiment are summarized in Table 1. Each experiment utilized two nested domains (D01 and D02), with the outer domain D01 having a coarser resolution (30 ~~m~~ meters or 90 ~~m~~meters) and using periodic boundary conditions on all sides, and the inner ~~domains~~ domain D02 (10 ~~m~~ meters or 30 ~~m~~meters) applying cell perturbation at the inflow boundary on the ~~east~~ west side. All domains except the ~~10-m~~ 10-meter domain had an aspect ratio of 2:1. The ~~10-m~~ 10-meter domain had a longer aspect ratio of 2.76:1 to allow the turbulence and turbine wake to evolve over a longer

225   distance.

The ~~model top~~ top model level for all experiments is set at 1600 ~~m~~meters, with an ~~800-m~~ 800-meter Rayleigh damping layer at the top with a coefficient of 0.2 s^{-1}. There is no vertical level stretching for the ~~30-m~~ 30-meter resolution experiments. In the case of the ~~10-m~~ 10-meter experiments, the vertical levels are stretched such that the near-surface vertical resolution is roughly 10 m. The initial potential temperature is 288 K from the surface up to 500 m, and then increases with a lapse rate of

230   1 K/100 m. We configured an idealized weak convective boundary layer with a surface turbulence heat flux of $\overline{(\theta'w')}_s = 0.02$ ~~W m s^{-2}~~ K m s^{-1}, similar to some previous studies (Muñoz-Esparza et al., 2014; Kale et al., 2022). After a spin-up time of ~~24~~ 20 hours, which is performed for the outer domain only, a quasi-equilibrium, well-mixed boundary layer is established. In order to have the wind in the boundary layer roughly in the zonal direction, the geostrophic wind is set to rotate slightly to the left, specifically, ~~$U_g = 9.91$ m~~ $U_g = 10.24$ m/s s^{-1} and ~~$V_g = -1.33$~~ $V_g = -1.39$ m s^{-1}. After the spin-up time, both domains

235   are integrated for ~~5~~ 4 hours with a 1-minute output interval for the inner domain (D02) for further analysis.

In our idealized experiments, no moisture is initialized. Except for the surface layer, all other physical parameterization schemes, including microphysics, cumulus, boundary layer, and radiation, are turned off. For the surface layer parameterization, we used the Revised MM5 Monin-Obukhov surface layer scheme (Jiménez et al., 2012). Similar to the idealized experiment, to enable the LES mode, we used the 1.5-order three-dimensional LES turbulence closure, in which the ~~sub-grid~~ subgrid-scale TKE is treated as a prognostic variable (Lilly, 1967). Other settings include: the Coriolis parameters are set to $1.177 \times 10^{-4} \mathrm{s}^{-1}$ (54°N), and the surface roughness length is set to 1 mm.

~~Power, thrust coefficient (C_t), and power coefficient (C_p) as functions of ambient wind speed (V_0) are shown for the 4 MW and 5 MW wind turbines used in the idealized (5 MW) and realistic (4 MW and 5 MW) experiments in this paper.~~

At the center of the inner domain, we placed a 5 MW wind turbine used at the Alpha Ventus wind farm. The turbine information taken from Larsén and Fischereit (2021) includes a rotor diameter of 116 m, a hub height of 90 m, and the thrust and power ~~coefficient~~ curves at different wind ~~speed~~ speeds (Fig. 2).

PALM configurations

To evaluate the performance of the SADLES module in simulating turbine wakes, we compared the results from the WRF-SADLES model with those from the ~~Parallelized Large-eddy Simulation Model (PALM, Maronga et al., 2015, 2020),~~ PALM model, maronga2015parallelized,maronga2020overview, system 21.10 revision r4901. PALM is an LES model developed at Leibniz Universität Hannover, Germany, and has been shown in several studies to be capable of simulating wind turbine wakes effectively (e.g. Witha et al., 2014; Vollmer et al., 2015).

~~The wind turbine in PALM (PALM-WTM)~~ In PALM, the wind turbine is represented by an advanced actuator disc with rotation, which calculates both the thrust and torque ~~force as a function~~ forces as functions of radius and tangential ~~distance from the rotor center~~ angle from the center of the rotor. Similar to the GAD methods (Mirocha et al., 2014; Kale et al., 2022), ~~PALM-WTM~~ the wind turbine model in PALM computes the local lift and drag forces based on the ~~Blade Element Momentum (BEM)~~ BEM method, which is accurate but requires additional information on the turbine and blade aerodynamic properties. For this reason, currently only ~~two~~ three types of wind turbines are officially supported, including the National Renewable Energy Laboratory (NREL) 2.3-MW, 5-MW and 15-MW models ~~(Jonkman et al., 2009; Gaertner et al., 2020)~~ (Jonkman et al., 2009; Gaertner et al., 2020; Ardillon et al., 2023). To compare with WRF-SADLES, we used the NREL 5-MW model with the same hub height of 90 m. However, the rotor diameter of the NREL 5-MW is slightly larger at 128 ~~m~~ meters compared to the ~~116 m~~ 116-meter diameter of the 5-MW turbine used in WRF-SADLES.

~~We design~~ The two idealized experiments, P10m and P30m, with two nested domains similar to the ~~WRF~~ WRF-SADLES experiments (see Table 1 for domains configurations). Cyclic lateral boundary conditions were used for the coarser domain. To prepare initial conditions for the main run we used a precursor run. Precursor domains are very smaller than main simulations. It has been defined 96×64 grid points for both 30m and 10m simulations in precursor run. Number of vertical levels for each precursor run is the same as the main run. The model has implemented for 86400 seconds to reach a steady state condition in precursor mode. To parameterize subgrid-scale (SGS) turbulence in PALM we used 1.5-order closure (according to Deardorff (1980) and modified by Moeng and Wyngaard (1988) and Saiki et al. (2000)). ~~The same atmospheric conditions~~

270   ~~as~~ We considered atmospheric conditions similar to those in the WRF model~~were considered. Initial potential temperature is~~, including: an initial potential temperature of 288 K, a surface turbulence heat flux of $\overline{(\theta'w')_s} = 0.02$ W m^{-2}, ~~the geostrophic wind is about~~ and a geostrophic wind of approximately 10 m/s from the west.

3.2 Result
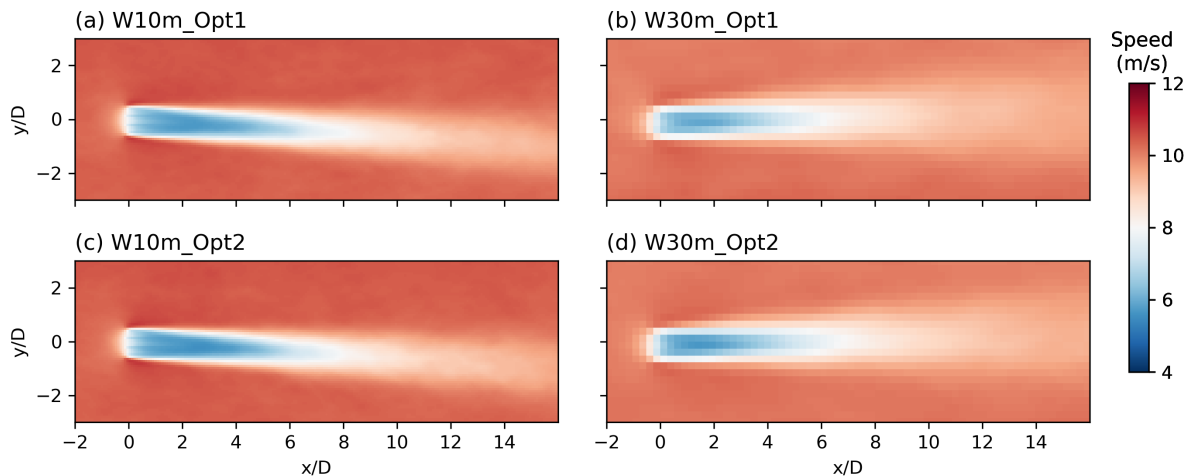
Figure 3. ~~Snapshot at 60 minute of~~ 4-hour average wind ~~speed~~ speeds at the turbine hub height (90 m) ~~for~~ from idealized ~~LES simulation using PALM (a,b) and~~ WRF-SADLES ~~(c,d-Option 1; e,f-Option 2) . For comparison, all the domains is zoomed to the WRF's 10-m resolution domain. The vertical dashed lines show the locations~~ simulations with different resolutions and options ~~for the spectral analysis in Fig~~ for axial induction factors.~~8~~

Figure ~~??~~ ~~illustrates the instantaneous hub-height wind speed after 60 minutes of simulation for all experiments. In the 10-m~~
275   ~~resolution experiments, a distinct wake from the turbine is visible and is similar in both the PALM and~~ 3 shows the average wind speeds over 4 hours for the four WRF-SADLES ~~experiments. The wake extends from the rotor and stretches over a distance of 1500 m (or 13 turbine diameters), exhibiting some small-scale meandering. Inside the wake,~~ idealized experiments, varying in resolutions and axial induction options. Noticeably, the averaged wake angles, reflecting average wind direction, differ between the 10-meter and 30-meter resolutions, suggesting a dependency of momentum fluxes on model solutions. Furthermore, the
280   10-meter resolution experiments exhibit slower wake recovery and a smaller rate of wake expansion, indicating potentially stronger turbulence activities at lower resolutions. Conversely, minimal difference is observed between the two options for calculating the axial induction factor, with visually identical averaged wind speeds. This validates the 1-D momentum theory of the actuator disc, which is used for calculating axial induction factor a. Given that Option 1 necessitates wind speed evaluation in front of the ~~wind speed drops to below 5 m/s, compared to the ambient wind speed of approximately 10 m/s outside of the~~
285   ~~wake. Compared to the 10-m resolution experiments, the wake is less clear in the 30-m resolution experiments. It also appears that the wake recovery is slower in the PALM experiment (P30m)~~ turbine, it may be sensitive to model resolution and blockage

effects. Therefore, we recommend the use of Option 2 in practical applications. Subsequent sections will explore the effect of the added TKE source and compare WRF-SADLES simulations with PALM simulations.

~~In both the PALM~~
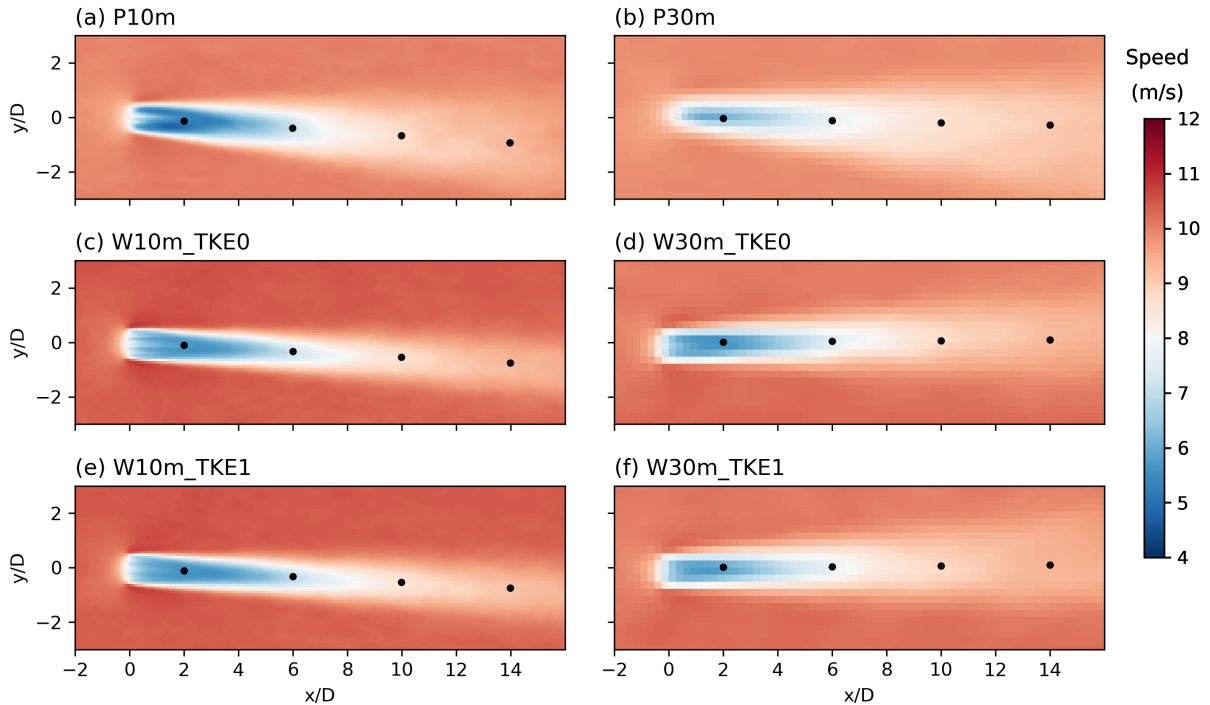
Figure 4. Similar to Fig. 3, but for PALM simulations and WRF-SADLES simulations with different f_{TKE} values (=0 for _TKE0, =1 for _TKE1). Black dots indicate distances of $2D$, $6D$, $10D$, and $14D$ behind the turbine.

290   Figure 4 depicts a comparison of the averaged wind speeds between PALM simulations and WRF-SADLES ~~experiments, there are elongated features that can be seen in the turbulence~~ with $f_{TKE} = 0$ or 1. Interestingly, for the same resolution, minimal variation is observed in the WRF-SADLES experiment, indicating that the wake may not be significantly affected by the added subgrid-scale TKE at the actuator disk. However, ~~there appears to be turbulent-free regions between these features in the PALM experiments, while there is intermediate turbulence present in between these features in the~~ a more noticeable

295   difference is evident between WRF-SADLES ~~experiments. This is likely due to the cell perturbation at the inflow boundary, which causes the turbulence in the WRF-SADLES experiments to fully develop quickly before reaching the wind turbine located at the center of the domain~~ and PALM. This disparity could be attributed, at least in part, to methodological differences (e.g., simple actuator disk versus actuator disk with rotation) and potentially differing turbine properties.

~~Power spectral density of wind speed for PALM and WRF-SADLES at 500m in front of the turbine (shown with solid lines)~~

300 ~~and 1500 m behind the turbine (shown with dashed lines).~~

~~The time-averaged power spectral densities (PSDs) of the two models (shown in Figure 8) are similar , particularly in the 10-m resolution experiments. In both models, the $-5/3$ Kolmogorov power law is only applicable to ashort range of wave numbers (from 2×10^{-3} m~~Both the PALM and WRF-SADLES simulations show similar wake shapes at the 10-meter resolution (Fig. 4 a, c, e). However, near the turbine, PALM predicts a lower wind speed of around 4 m s^{-1} ~~to $\times 10^{-2}$ m^{-1}, or wave lengths from 100 m to 500 m)~~for the 10-m experiments. ~~In comparison, the 30-m resolution experiments have a higher PSD than the 10-m resolution experiments for wave numbers less than 3×10^{-3} m^{-1} (corresponding to wave lengths of about 300 m), but the PSDs quickly decrease for higher wave numbers.~~

~~There are some differences in the PSDs of the two models. One notable difference is that the PSDs of the~~ compared to WRF-SADLES~~decrease more quickly for wave numbers higher than 3×10^{-3} m'~~ 6 m s^{-1}in the 30-m resolution experiments. ~~Secondly,~~. Additionally, the wake ~~in the PALM experiments, the PSDs evaluated 1500 m behind the turbine are slightly higher than those evaluated 500 m in front of~~ simulation expands slightly with increasing distance from the turbine, ~~suggesting that the turbine model has increased the explicit turbulence. However, in the~~ while WRF-SADLES ~~experiments, the turbine has little effect on the explicit turbulence due to the lack of consideration for tangential effects, as indicated by the small difference in the PSDs behind and in front of the turbine~~exhibits minimal expansion. This difference might be attributed to the absence of the rotational effect in WRF-SADLES, which is included in PALM.

~~4-hour average wind speeds at the turbine hub height (90 m) for idealized LES simulations using PALM (shown in panels a and b) and WRF-SADLES (shown in panels c and d for Option 1, and panels e and f for Option 2). The dots indicate the locations of 2D, 4D, 8D, and 12D, which are used for evaluating the wake deficit in Figure 5.~~

~~Figure ?? shows the average wind speeds over a 4-hour period for all of the idealized experiments. It can be seen that the averaged wakes are not perfectly aligned in the zonal (west-east) direction because the quasi-equilibrium states depend on the momentum fluxes of eddy activities, which may vary slightly between different models and resolutions. In the 10-m resolution experiments, the wake intensity appears to be slightly stronger in the PALM simulations~~ At the 30-meter resolution (Fig. 4b, d, f), WRF-SADLES shows consistent wake intensity and shape compared to the ~~WRF-SADLES simulations, which could be due to differences in the methods and turbine configurations used~~10-meter results. However, ~~when comparing the 30-m resolution simulations to the 10-m resolution simulations, the WRF-SADLES experiments show better agreement than the PALM experiments. The 30-m resolution simulation of PALM (shown in Figure ??b) has a less distinct, but longer, stretched wake. There is also good agreement between the two SADLES options (shown in Fig. ??c,d and Fig. ??e,f), which confirms the validity of the 1-D momentum theory~~the wake in PALM experiment at 30-meter resolution (Fig. 4b) is much weaker and narrower than in at 10-meter resolution. The cause of this discrepancy is unclear, but one possibility is related to the interpolation between the actuator disc polar grid system and the Cartesian coordinate system used in the PALM model.

We calculated the vertical wake deficit at distances behind the turbine of two turbine diameters ($2D$), $6D$, $10D$, and $14D$ (as shown in ~~Figure 5). The positions where the wake deficit was calculated are indicated by the black dots in Figure ??. Because the average wake axes are not perfectly aligned in the zonal direction, we did not use the (x, z)-cross section output of the PALM model, but instead calculated the wake deficit from the 3D outputs, which have limited vertical levels (shown by dots in~~Fig. 5).
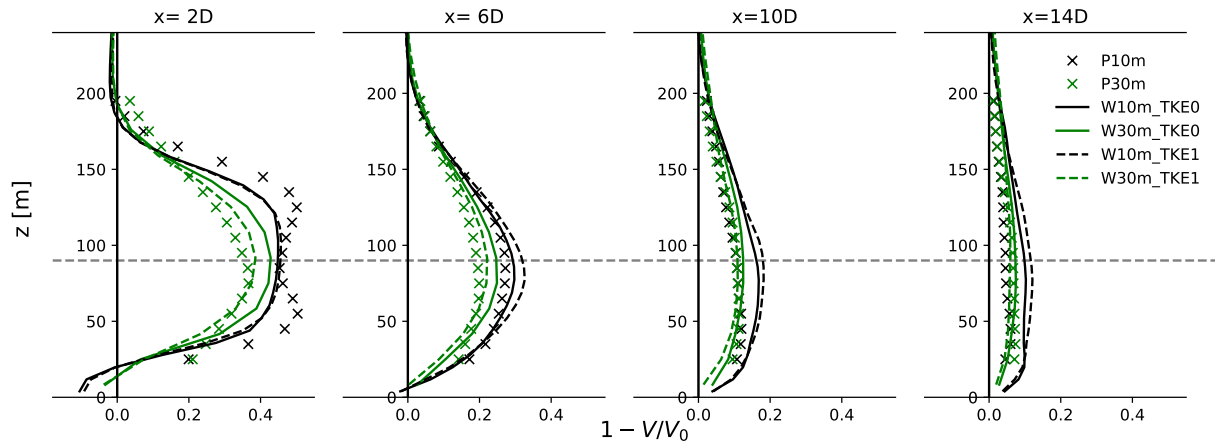
Figure 5. Vertical wake deficit $(1 - V/V_0)$ for idealized ~~experiments~~ at distances behind the turbine of two turbine diameters $(2D)$, $6D$, $10D$, and $14D$. The evaluation points are indicated by black dots in Fig. ~~??~~4.

At the near-wake distance of ~~two turbine diameters ($2D$),~~ the wake deficits agree at around 50% for both PALM and WRF-SADLES~~, the wake 10-m simulations have a slightly stronger wake deficit compared to the 30-m simulations~~. However, the P10m ~~has a lower deficit near~~ deficit exhibits a distinct shape with two peaks, one above and one below the hub height~~because~~, due to the nature of the BEM method~~used in PALM. This feature does not present in WRF-SADLES and also in P30m because~~ 340 ~~of the resolution limitation~~. At 30 meters, the wake deficit is weaker for both models, though the W30m_TKE0 experiment shows the closest agreement to the higher-resolution simulations.

~~At a distance of two turbine diameters~~ As the distance from the turbine ~~(near-wake)~~increases, both the PALM and WRF-SADLES ~~simulations with a 10-m resolution show a slightly stronger wake deficit compared to the simulations with a 30-m resolution~~models show similar wake deficit profiles with a single peak located slightly below the hub height. However, 345 their wake recovery rates differ. In the PALM simulations, the 10-meter resolution wake recovers faster than the 30-meter one, resulting in a larger deficit at 14D for the P30m simulation. Conversely, the ~~PALM simulation with a 10-m resolution (~~WRF-SADLES wakes recover slower at 10 meters, leading to consistently higher deficits compared to the 30-meter simulations. Interestingly, using the P10m ~~) has a lower deficit near the hub height, which is likely due to~~ simulation as a reference, the WRF-SADLES simulation without added subgrid-scale turbulence (W10_TKE0) shows better agreement than the one with 350 added TKE (W10_TKE1). While W10_TKE0 aligns better at near-wake distances, the ~~BEM method used in PALM. This feature is not present in the WRF-SADLES simulations or in the PALM simulation with a 30-m resolution (P30m), which may be due to the resolution limitation. As the distance from the turbine increases, this feature disappears and the deficit shapes of the two models become similar. The wake deficit for the higher-resolution simulations (10-m) recovers faster than the lower-resolution simulations (30-m) , which may be due to the effect of explicit turbulence , which is weaker for lower~~ 355 ~~resolutions. However, at a far wake distance (~~30-meter simulation without added TKE (W30_TKE0) exhibits better agreement at far-wake distances (10D ~~), the~~ and 14D).
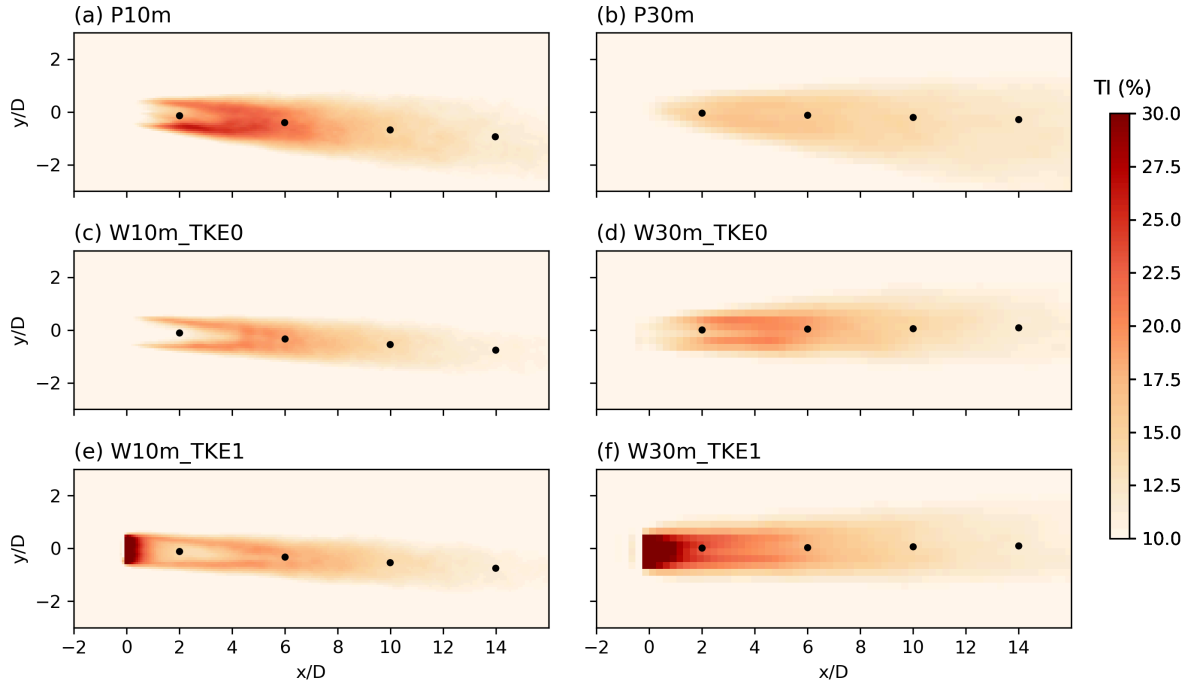
Figure 6. Similar to Fig. 4, but for the time-averaged turbulence intensity $\overline{TI}$.

To gain insight into why the added subgrid-scale TKE source has minimal impact on the wake in WRF-SADLES, we compared the calculated average turbulence intensity (TI) between the experiments. The average TI is computed using the equation:

$$\overline{TI} = \frac{\sqrt{\frac{2}{3}\overline{TKE}}}{|\mathbf{V}|},$$

(8)

where $\overline{TKE}$ represents the time-averaged total turbulence kinetic energy, is the sum of gridscale ($\overline{TKE}_{gs}$) and subgrid-scale ($\overline{TKE}_{sgs}$) terms. $\overline{TKE}_{sgs}$ is a prognostic variable derived from the 1.5-order turbulence closure within the PALM and WRF-SADLES ~~simulations of two resolutions agree slightly better than the PALM simulation, which is likely due to~~ models. On the other hand, the gridscale term is derived from $\overline{TKE}_{gs} = \frac{1}{2}(\overline{u'^2} + \overline{v'^2} + \overline{w'^2})$, where u', v', w' denote the deviations of wind speed components from their respective time averages over the simulation period.

Figure 6 compares the average TI at the ~~sub-grid turbulent effects from the TKE production of SADLES~~ hub height for the PALM and WRF-SADLES simulations, including cases with and without added subgrid-scale TKE sources in WRF-SADLES. Outside the wake regions, all experiments show a consistent TI of around 10%. Both the PALM and WRF-SADLES simulations exhibit TI development at the turbine edges due to shear production. The maximum TI reaches approximately 20% at distances

370 ~~beyond~~ 2D. In contrast, the WRF-SADLES experiment with added subgrid-scale TKE (_TKE1) achieves the intended effect, with a maximum TI exceeding 30% at the turbine location. However, this additional subgrid turbulence quickly dissipates as it advects downstream. Within about $2D$ for W10m_TKE1 and $4D$ for W30m_TKE1, the TI levels in the simulations with added subgrid-scale TKE become comparable to those without.
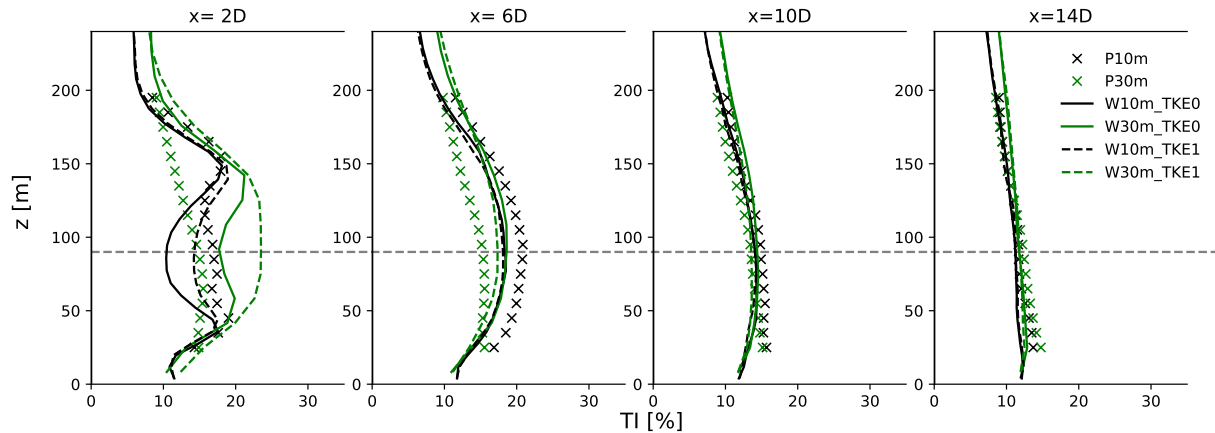
Figure 7. ~~Box plots of ambient wind speed (a) and turbine power (b)~~ Similar to Fig. 5 but for the ~~WRF-SADLES experiments are shown~~time averaged turbulence intensity $\overline{TI}$.~~In each panel, the average of all experiments is indicated by a dashed line for comparison.~~

Figure~~??a shows the box plots of the ambient wind speeds for the~~ 7 presents the vertical structure of the time-averaged
375 turbulent intensity (TI) at various distances behind the wind turbine. Significant discrepancies in the TI are observed between the two models (PALM and WRF-SADLES~~experiments. For direct evaluation (Option 1) of the ambient wind speed, there is a slight difference of approximately 0.15 m/s in the average wind speed for the resolutions of~~) and resolutions (10 ~~m~~meters and 30 ~~m. This is~~meters) at the near-wake distance of $2D$. The experiments with 10-meter resolution show two TI peaks above and below the hub height, likely due to ~~differences in eddy fluxes. When it comes to the inferred evaluation of~~ the ~~ambient~~
380 ~~wind speed (Option 2), the difference between the two resolutions is slightly larger, at about 0.3 m/s. Both of these differences are relatively small, representing about 1.5%~~ shear production of turbulence. These peaks reach a TI of about 20% and are consistent between the PALM and WRF-SADLES models. The WRF-SADLES model with added subgrid-scale TKE shows a TI about 5% higher than the non-added TKE counterpart. The W30m_TKE1 experiment has the highest TI value, reaching approximately 25%.

385 Beyond $6D$ downstream, both resolutions of the WRF-SADLES simulations show consistent TI predictions. However, discrepancies remain between the 10-meter and ~~3% of the ambient wind speed, respectively. However, due to the non-linear relationship,~~ 30-meter resolutions in the PALM simulations. The 30-meter PALM experiment exhibits a significantly lower TI compared to all others, while the 10-meter version shows the highest TI. As the wake recovers further downstream, the TI variations across all simulations weaken. This weakening of wake turbulence brings them closer to background levels, typically
390 around 10% near the hub height and decreasing with height. This convergence typically occurs by 14D downstream.

Using the 10-meter PALM simulation as a reference, the ~~differences in~~ WRF-SADLES model displays a similar TI structure, especially at far-wake distances. Adding a tendency term for subgrid-scale TKE in WRF-SADLES primarily impacts the near-wake region and has minimal effect further downstream. For both near and far wakes, the ~~turbine power (Figure ??b) are larger, at 4% for Option 1 and 8% for Option 2. Compared to the average wind speed and turbine power of Option 1 and~~ Option 2, Option 2 is larger for the 10 m resolution , but smaller for the 30-m experiments without added subgrid-scale TKE in WRF-SADLES show better agreement with the reference experiment for both resolutions (30-meter and 10-meter). Therefore, we recommend using the WRF-SADLES model without the added subgrid-scale TKE source (i.e., $f_{TKE} = 0$) in practical applications.
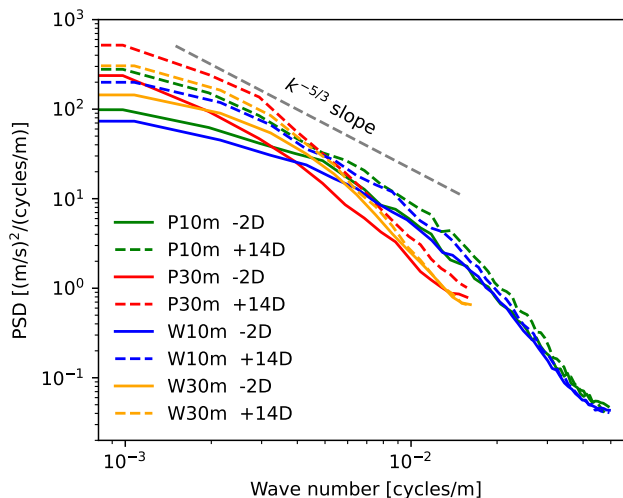
Figure 8. Time-averaged power spectral densities (PSDs) of wind speed spatial fluctuations for the PALM (P10m, P30m) and WRF-SADLES (W10m, W30m) simulations at two locations: $-2D$ upstream and $+14D$ downstream of the wind turbine. The analysis was computed from a meridional cross-section at hub height with a length of $8D$, centered on the wake axis.

To further assess the turbine's influence on turbulence, we analyzed the time-averaged wavenumber power spectral densities (PSDs) at $2D$ upstream and $14D$ downstream, revealing the turbulence characteristics at pre-wake and post-wake distances, respectively (Fig. 8). For consistent comparisons across simulations, the wavenumber spectral analysis was conducted in a meridional cross-section at hub height with a length of $8D$. To improve clarity and avoid redundancy, we present the average results of all WRF-SADLES simulations at each resolution (W30m and W10m for 30-meter and 10-meter resolutions, respectively) since their turbulence properties exhibit minimal variation across different options within the model.

Both WRF-SADLES and PALM simulations exhibit similar trends in turbulence properties. Simulations with a 10-meter resolution capture higher turbulence levels, particularly for smaller-scale structures (wavenumbers above 4×10^{-3} cycles/m, corresponding to wavelengths shorter than 250 meters). This indicates a better ability to resolve these structures with finer resolution.

4 ~~Example 2: Real data meso-to-micro nesting simulation~~

3.1 ~~Model configurations~~

~~WRF domain configurations for the real-data downscaling experiments. Domain $N_x \times N_y \times N_z$ Δx (m) Δt s L_x km L_y km D01 385 × 321 × 60 9000 45 3456 2880 D02 481 × 382 × 60 3000 15 1440 1143 D03 322 × 322 × 60 1000 5 321 321 D04 321 × 321 × 60 200 1 64 64 D05 481 × 481 × 60 40 1~~ The 30-meter simulations show a faster dissipation of turbulence energy compared to the Kolmogorov power law (represented by a -5/~~5 19.2 19.2~~ 3 slope) at smaller scales (wavenumbers above 4×10^{-3} cycles/m). This suggests limitations in capturing the energy transfer mechanisms at these scales. In contrast, the 10-meter simulations exhibit a broader range of applicability for the Kolmogorov power law, spanning from approximately 2×10^{-3} to 10^{-3} cycles/m (corresponding to wavelengths between 100 meters and 500 meters). This wider range signifies a more accurate representation of the energy cascade across different scales in these simulations.

~~WRF domains used for example 2. The first three domains (a) are the mesoscale or Reynolds-averaged Navier–Stokes (RANS) domains. The two innermost domains (b) are the LES domains. See Table 2 for detailed domains dimensions. The terrain map was generated using data from Stamen Design with a Creative Commons Attribution (CC BY 3.0) license.~~

~~In this example, we used the~~ Furthermore, all simulations show an increase in turbulence energy at the far-wake distance $(14D)$ compared to upstream turbulence $(-2D)$, for all wavenumbers. This increase is more pronounced for lower wavenumbers (longer wavelengths) than for higher wavenumbers. This behavior is consistent for both PALM and WRF-SADLES ~~system to downscale the ERA5~~ models.

4 Meso-to-micro realistic downscaling simulation

This section demonstrates meso-to-micro downscaling using global reanalysis data ~~(Hersbach et al., 2020). The~~. We employ the ERA5 data ~~has a~~ set from the European Centre for Medium-Range Weather Forecasts (ECMWF) (Hersbach et al., 2020). This data has a spatial resolution of approximately 31 ~~km~~ kilometers and is available ~~on an hourlybasis. To achieve a~~ hourly. First, we briefly compare the simulation results with observational data from the FINO1 meteorological station in the southern North Sea. This comparison aims to assess the model's ability to reproduce real-world conditions. Subsequently, we will provide an example illustrating power loss due to farm-to-farm interaction.

4.1 Model configurations

To achieve turbine-scale resolution ~~of 40 m, we used~~, we employed a system of five nested domains (~~as shown in Table~~ detailed in Table 2). Each domain progressively reduces its grid size for finer resolution. The first three domains (D01, D02, D03; see Fig. 9a) focus on downscaling the mesoscale processes, while the final two domains (D04, D05; see Fig. 9b) transition to Large Eddy Simulation (LES) for high-resolution wind flow near the turbines.

The outermost domain (D01) ~~had~~ has a resolution of 9 ~~km and covered a large region including~~ kilometers, encompassing a vast region that includes Europe and the North-East Atlantic Ocean ~~, while the~~ (Figure 9a). The second domain (D02)

zooms in on the North Sea (Figure 9a). The remaining three domains are centered around the Alpha Ventus wind farm, located near the FINO1 meteorological mast station (Figure 9b).

The first LES domain (D04) has a resolution of 200 meters and acts as an intermediate step between the meso-scale and turbine-scale domains. It does not include wind turbines within its simulation. The innermost domain (D05) has the highest resolution of 40 meters and encompasses a smaller area (19.2 km × 19.2 km) compared to a single grid cell of the original ERA5 data. This is the domain where the SADLES model is activated for simulating turbine wakes.

In domain D05, four wind farms are present comprising 5-MW and 4-MW turbines. Notably, the Alpha Ventus wind farm, featuring twelve turbines, is situated to the right of the FINO1 mast station. Detailed turbine specifications, including power and thrust curves, can be referenced in Larsén and Fischereit (2021) (refer to Fig. 2).

For the subsequent experiments, we adopted the SADLES Option 2 for the inferred evaluation of the axial induction factor, along with the f_{TKE} value of 0.

For vertical grid resolution, we adopted 60 levels following Bui and Bakhoday-Paskyabi (2022). This setup provides high resolution near the surface, approximately 10 meters, with 21 levels below 500 meters height. Regarding physical parameterization, we employed the following options: the RRTMG (Rapid Radiative Transfer Model for General Circulation Models) scheme (Iacono et al., 2008) for radiation parameterization across all domains, the Thompson graupel scheme (Thompson et al., 2008) for microphysics parameterization. The Tiedtke scheme (Zhang et al., 2011) was utilized for cumulus parameterization in the outermost 9-km domain (D01), with cumulus parameterization disabled in finer resolution domains. For surface layer parameterization, we utilized the Monin-Obukhov Similarity scheme (Jiménez et al., 2012), and the Noah Land Surface Model (Mukul Tewari et al., 2004) was employed for land surface parameterization in all domains. The Yonsei University (YSU) scheme (Hong et al., 2006) was chosen for PBL parameterization in mesoscale domains (D01-D03), while PBL parameterization was disabled in LES (Large Eddy Simulation) domains (D04, D05). To simulate large eddies in LES domains, we employed the 1.5-order three-dimensional TKE closure (Lilly, 1967), supplemented by the

Table 2. WRF domain configurations for the real-data downscaling experiments.

Domain	$N_x \times N_y \times N_z$	Δx (m)	Δt [s]	L_x [km]	L_y [km]
D01	$385 \times 321 \times 60$	9000	45	3456	2880
D02	$481 \times 382 \times 60$	3000	15	1440	1143
D03	$322 \times 322 \times 60$	1000	5	321	321
D04	$321 \times 321 \times 60$	200	1	64	64
D05	$481 \times 481 \times 60$	40	1/5	19.2	19.2

cell perturbation method ~~is applied to~~ along the southern and western boundaries for the first 16 levels from the surface (up to
475 approximately 300-meter height) to initiate turbulence development.
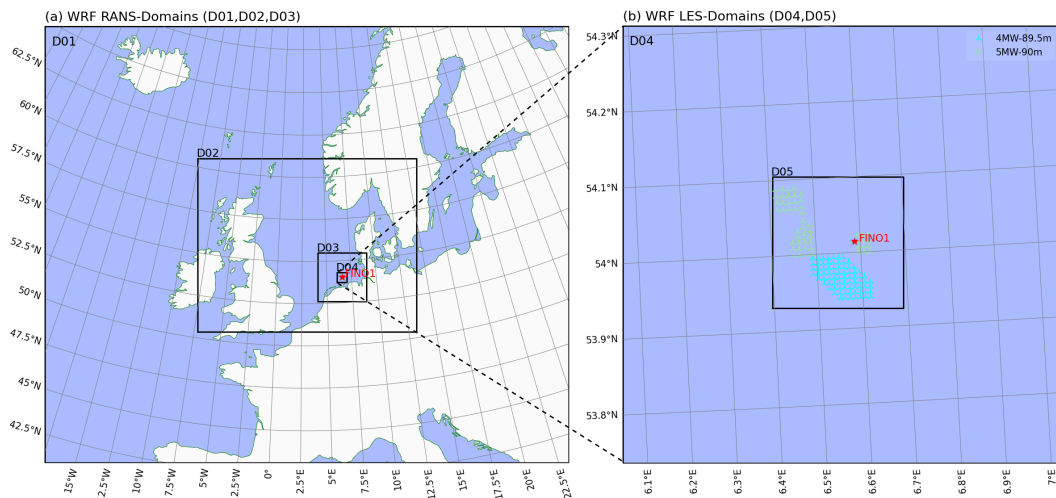
Figure 9. WRF domains used in the meso-to-micro downscaling simulations. The first three domains (a, D01-D03) are for mesoscale simulations, while the two innermost domains (b, D04, D05) are for LES simulations. The SADLES model is enabled in D05, with wind turbine locations marked by green and cyan markers. The FINO1 meteorological mast station is indicated by the red star. Refer to Table 2 for detailed domain dimensions.

4.2   Comparison with observational data

This section briefly evaluates the performance of WRF-SADLES using observations from the FINO1 meteorological mast station. We compare wind speed and direction data collected by cup anemometers at 90 meters (hereafter referred to as "mast data") with WRF-SADLES simulations. Additionally, we utilize data from a Windcube© 100s wind LiDAR (Kumer et al., 2014)
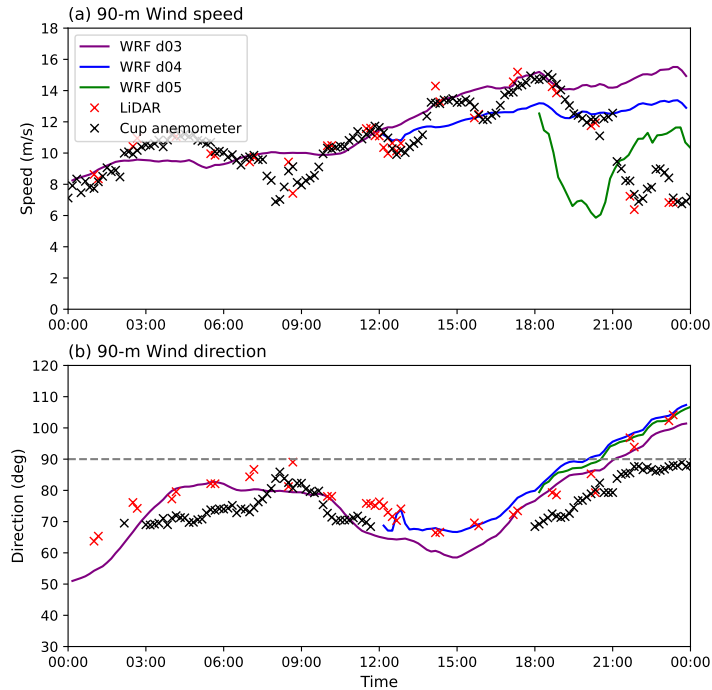
Figure 10. Time series of hub-height wind speed (a) and wind direction (b) at the FINO1 met-mast station on August 13, 2015, from 00:00 to 24:00 UTC, alongside data from WRF-meso (d01), WRF-LES (d02), WRF-SADLES (d03), LiDAR, and cup anemometers (Mast).

480 (hereafter referred to as "LiDAR data"). The LiDAR data provides vertical profiles of wind speed and direction from vertical scans, along with radial wind speed from horizontal scans.

The simulation period spans from 00:00 to ~~a height of about 300~~ 24:00 UTC on August 12, 2015. During this time frame, the first three domains (D01, D02, D03) run from 00:00 to establish mesoscale conditions, while the 200-meter WRF-LES domain (D04) begins at 12:00 UTC to serve as an intermediary between meso- and micro-scales. Finally, the 40-meter WRF-SADLES

485 domain starts at 18:00 UTC to simulate turbine wakes. This period was selected because, towards its end, the wind direction shifts eastward, allowing for observation of wake effects using measurement data from the Fino1 station. Additionally, a low-level jet (LLJ), characterized by maximum wind speeds within the atmospheric boundary layer (ABL), is also observed during this timeframe.

Figure 10 compares wind speed and wind direction at 90 meters (hub height of the 5-MW Alpha Ventus wind turbines) from

490 WRF simulations (D03: WRF-meso, D04: WRF-LES, and D05: WRF-SADLES) with observations from the FINO1 mast. Observations from both the mast data and LiDAR data suggest the wake effect from nearby turbines partially reduces wind speeds around 9:00, 13:00, 17:00, and 19:00 UTC, with reductions of approximately 2 m~)~/s. From 22:00 onwards, the wakes

exhibit a full effect, particularly when the wind direction approaches easterly (90 degrees), with wind speeds reduced from 6 to ~~trigger the development of turbulence.~~ 8 m/s. While both data sources show good agreement in wind speed, there is a consistent difference of around 10 degrees in wind direction between the mast data and LiDAR data.

4.3 ~~Result~~

After a few hours of spin-up time, WRF-meso wind speeds agree well with observations when wakes do not affect the location. However, the intermediate LES domain (D05) underestimates wind speeds by about 2 m/s. Without the inclusion of the wind turbine model, neither WRF-meso nor WRF-LES captures the wake effect at the FINO1 location. In contrast, WRF-SADLES, which includes a wind turbine model, successfully simulates the full wake effect at FINO1. Wind speeds are reduced to around 6 m/s, aligning well with observations. However, the timing of the wake impact differs, occurring between 19:00 and 21:00 UTC, roughly 2 hours earlier than observed.

To gain a clearer understanding of the discrepancies between WRF-SADLES simulations and observations, we examine the vertical profiles of wind speed (Fig. 11a) and wind direction (Fig. 11b) at two key points in time. The first is 20:30 UTC when the WRF-SADLES simulation shows the full wake effect. The second is 22:00 UTC when the full wake effect is observed in the data. At both times, the LiDAR data reveals a Low-Level Jet (LLJ) structure with a wind speed maximum of 17-20 m/s at around 300 meters. The observations of wind direction indicate wind veering, where the wind direction consistently turns clockwise with increasing height. However, within the overlapping region from 90 to 150 meters, some discrepancies exist between the two datasets. While the mast data exhibits consistency with the LiDAR data above 150 meters, the LiDAR wind directions below 150 meters may exhibit errors due to potential limitations in the retrieval algorithm or interference from the mast itself.

The mesoscale domain (D03) of the WRF model accurately replicates the observed LLJ) event, capturing both its magnitude and the height of the wind speed maximum. However, the WRF-LES and WRF-SADLES simulations produce a weaker LLJ, with wind speeds 2-3 m/s lower. In terms of wind direction, the observations exhibit the highest vertical wind veer (approximately 8 degrees per 100 meters), followed by the mesoscale simulation (around 6 degrees per 100 meters). The WRF-LES simulations show the weakest vertical wind veer (about 4 degrees per 100 meters). The WRF-SADLES domain D05 performs slightly better than the WRF-LES domain D04 in capturing both wind speed and direction.

The full wake effect is observed when the wind direction approaches 90 degrees (easterly). At such times, the wake from the nearest Alpha Ventus turbine to the east reaches the FINO1 mast station. This is evident in both the observational wind speed (combining LiDAR and mast data) and the WRF-SADLES simulation, which show dips in wind speed. Notably, the wind speed profiles from the simulation and observations exhibit visually similar structures.

Figure 12(b) shows a horizontal LiDAR scan from the FINO1 station at 23:00 UTC., at which the wind is blowing from the east and the full wake effect of a wind turbine from the Alpha Ventus is recorded. The LiDAR scan covers a circular sector extending from a height of 23.5 meters with a small elevation angle of 1.55 degrees, reaching a radius of 2500 meters and encompassing five turbines. The signal reaches a height of approximately 90 meters at the outer radius, corresponding to
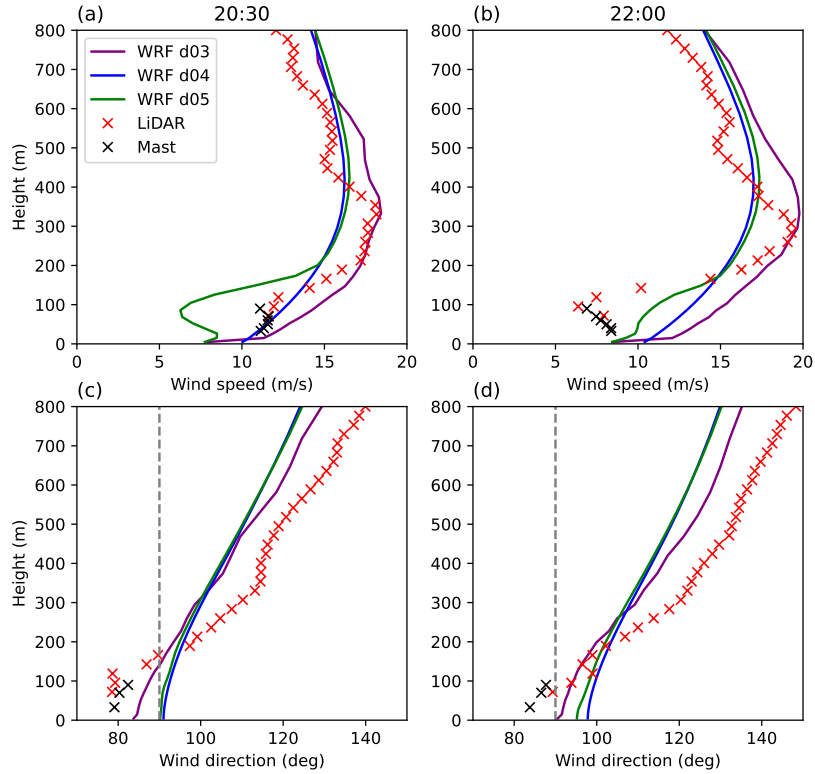
Figure 11. Vertical profiles of wind speed (a, b) and wind direction (c, d) recorded at the FINO1 met-mast station on August 13, 2015, at 20:30 UTC (a, c) and 22:00 UTC (b, d). The comparison includes data from WRF-meso (d01), WRF-LES (d02), WRF-SADLES (d03), LiDAR, and cup anemometers (Mast).

the hub height of the turbines. Turbine wakes are clearly visible, except for the middle turbine on the right, which is likely non-operational.

For comparison, in Fig. 12a, the simulated radial wind speed from the WRF-SADLES model at 23:00 UTC with an easterly wind direction is presented. Generally, there is good agreement between the model and LiDAR observations. Nevertheless, the WRF-SADLES wind speed distribution appears smoother due to its limited resolution compared to the LiDAR data

4.3 A brief example of farm-to-farm interaction

In this section, we briefly demonstrate the use of WRF-SADLES to simulate an example of farm-to-farm interaction. The LES simulations were conducted for domains D04 and D05 from 06:00 UTC to 12:00 UTC on September 24, 2016. The mesoscale domains commenced earlier at 00:00 UTC to initialize the environmental conditions. This timeframe was selected due to the
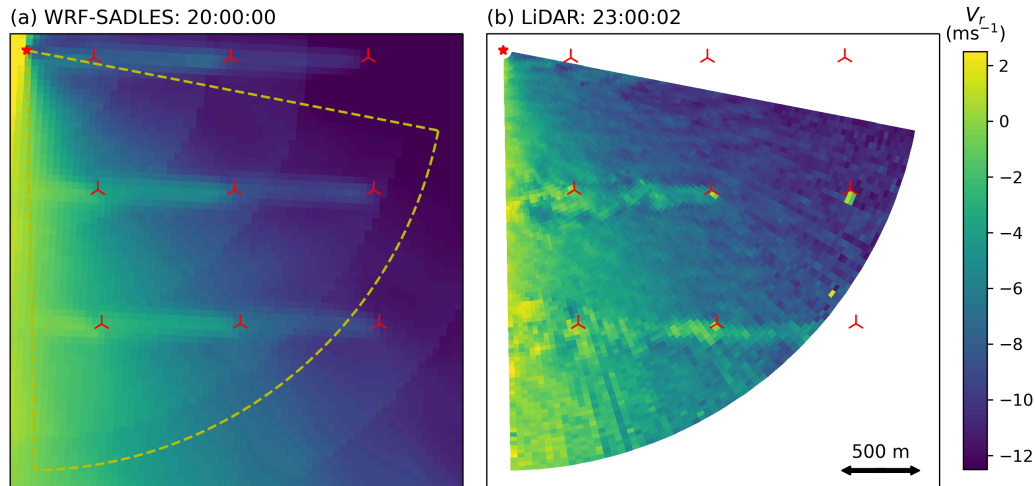
Figure 12. Radial wind speed from WRF-SADLES at 20:00 UTC (a) and horizontal LiDAR scans at the FINO1 station around 23:00 UTC (b).

relatively steady wind direction from the south-southwest, allowing farm-to-farm interactions between Alpha Ventus and the wind farm to the southwest. To quantify the influence of this farm, we set up two experiments: the first experiment (EXP1) incorporated all four wind farms, while the second experiment (EXP2) excluded all wind farms except Alpha Ventus.

Figure 13a and b shows an example snapshot of the wind speed at the Alpha Ventus ~~hub-height~~ hub height (90 m) for the ~~40-m~~ 40-meter LES domain for the two experiments at ~~08Z~~ 10:00 UTC on September 24, 2016. Thanks to the cell perturbation at the southern boundary, the turbulence quickly becomes fully developed after about two kilometers (or roughly ten percent of the domain width) from the southern border. This allows the turbulence flow to become quasi-steady when it reaches the turbines in the wind farms. Such turbulence development is important because it affects the wake recovery behind the turbines.

~~At the current time~~ Figure 13c and d shows the four-hour average wind speed from 08:00 to 12:00 UTC on September 24, 2016. During this time window, the wind direction is relatively steady from the South-Southwest, enabling us to address the potential impact of turbine wakes in the Alpha Ventus wind farm. Before coming to the ~~ambient wind speed is about 9 m/s, and the turbine wakes are clearly visible with a speed reduced to less than 5 m/s. The individual wakes have a stretch of about two kilometers. However, the imprint of the collective effect of the wind farmextends much further, covering more than half of the domain (or over ten kilometers). This collective effect of the~~ wind farm~~to the southwest of Alpha Ventus (Fig. 13) reduces the speed of the ambient flow compared to the case without the southwest wind farm . Thus we expect this farm-to-farm effects should reduce the extracted power of the Alpha Ventus.~~

~~The 5-hour average wind speed (from 07Z to 12Z on September 24, 2016) for the 40-m domain at a height of 90 meters for the two experiments in Example 2.~~
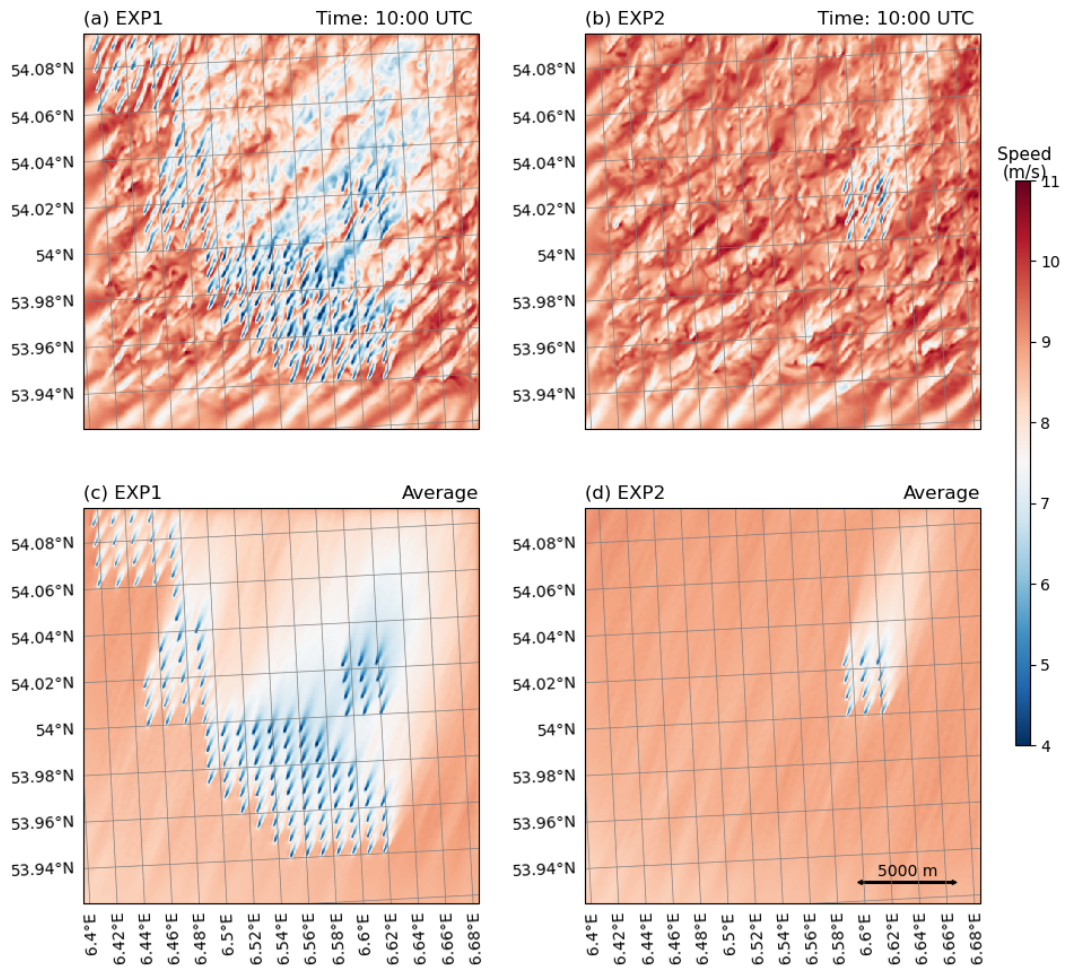
Figure 13. ~~The instantaneous~~ (a, b) A snapshot of wind speed in the ~~40-m~~ 40-meter domain (D05) at ~~a~~ the height of 90 meters at ~~08Z~~ 10:00 UTC on September 24, 2016; (c, ~~for the two experiments in Example 2.~~d) The 4-hour average wind speed (from 08:00 UTC to 12Z on September 24, 2016).

~~The five-hour average wind speed (from 07Z to 12Z on September 24, 2016) shows that the ambient wind is relatively steady~~ ~~during this period with an average wind speed of about~~ , the average speed is slightly above 8 m/~~s when it enters the domain~~
~~D05 (Fig. ??). Because of the south-southwest wind direction, the wake caused by the southwest wind farm causes the average~~
~~wind speed to reduce to about 6–7 m/s before it reaches~~ s and is distributed uniformly because of the small size of the domain.
In EXP1, the south-southwesterly wind direction and the wake from a nearby wind farm significantly reduce the wind speed
reaching Alpha Ventus (Fig. 13c). Conversely, with no upstream wind farm in EXP2, the averaged ambient wind speed remains
nearly unchanged when approaching the Alpha Ventus wind farm. ~~This causes the Alpha Ventus wakes to become more visible~~
~~in the case of~~ Consequently, the wake effect within Alpha Ventus is weaker in EXP1 ~~(with nearby wind farms) compared~~
~~with~~ compared to EXP2~~(without nearby wind farms). However, the effect of the intra-farm interaction within the Alpha Ventus~~
~~due to the wakes does not directly align with the downstream turbines of the next row~~. This highlights the significant impact
of farm-to-farm interaction, as evidenced by the larger difference in wind speed between the two scenarios compared to the
variation within Alpha Ventus itself. In both experiments, the collective wave effects from the wind farm reduce the average
wind speed to a distance over ten kilometers downstream.

~~Box plots of 5-hour ambient wind speeds (from 07Z to 12Z on September 24, 2016) for the turbines in the Alpha Ventus~~
~~wind farm. The average values (blue dashed lines) are 6.5 m/s and 7.6 m/s for (a) and (b) respectively. The layout of the turbines~~
~~in the Alpha Ventus wind farm is shown on the bottom right of panel (b).~~

~~The box plots in Fig. ?? also show that there is little~~ Both experiments also show evidence of some intra-farm interaction ~~in~~
~~the wind speeds experienced by the turbines . In the EXP1 experiments, there is no evidence of the wind speeds being reduced~~
where the wind speed deficits for turbines at the northeast corner are slightly smaller than those at the front south and west
sides. However, due to the specific wind direction, the wakes generated by the turbines ~~in~~ do not directly impact the turbines
in the following rows. Consequently, the ~~rows at the back. In fact, turbine T1 has the lowest average ambient wind speed ,~~
~~which may be due to the wake from a turbine in the southwest wind farm (see Fig. ??a). Similarly, in the EXP2 experiments,~~
~~the ambient wind speeds for each turbine are similar except for turbines T11 and T12 at the back row. These turbines likely~~
~~experience a reduction in wind speed due to the average wakes from turbines T1 and T2 in the front row, rather than from the~~
~~row directly in front of them (see Fig. ??b).~~ variation in wind speed deficit between turbines within the Alpha Ventus wind
farm is minimal compared to the overall difference between the two experiments.

Figure 14 also shows the intra-farm interaction is small compared to farm-tom-farm interaction. For each experiment, the
variation of the ambient wind speed is smaller than the difference between EXP1 and EXP2. The average ambient wind speed
at the Alpha Ventus wind farm is ~~lower when there are nearby wind farms present~~ significantly lower when the wind farm to
the south presents (EXP1) compared to when there are none ~~. When nearby wind farms (EXP1) are present~~(EXP2). For EXP1,
the average ambient wind speed is ~~6.5~~ 7 m/s, as shown in Fig. ~~??~~14a. In contrast, when there are no nearby wind farms (EXP2),
the average ambient wind speed is ~~7.6~~ 8.3 m/s, as shown in Fig. ~~??~~14b. This represents a reduction in wind speed of about
~~14~~16%. However, due to the non-linear nature of the turbine power curve, the power reduction resulting from the farm-to-farm
interaction (Fig. ~~??~~14) is larger. The average power for EXP2 is approximately ~~1.7~~2.25 MW, while the average power for
EXP1 is ~~1.1~~1.4 MW, corresponding to a reduction of about ~~35~~38%.
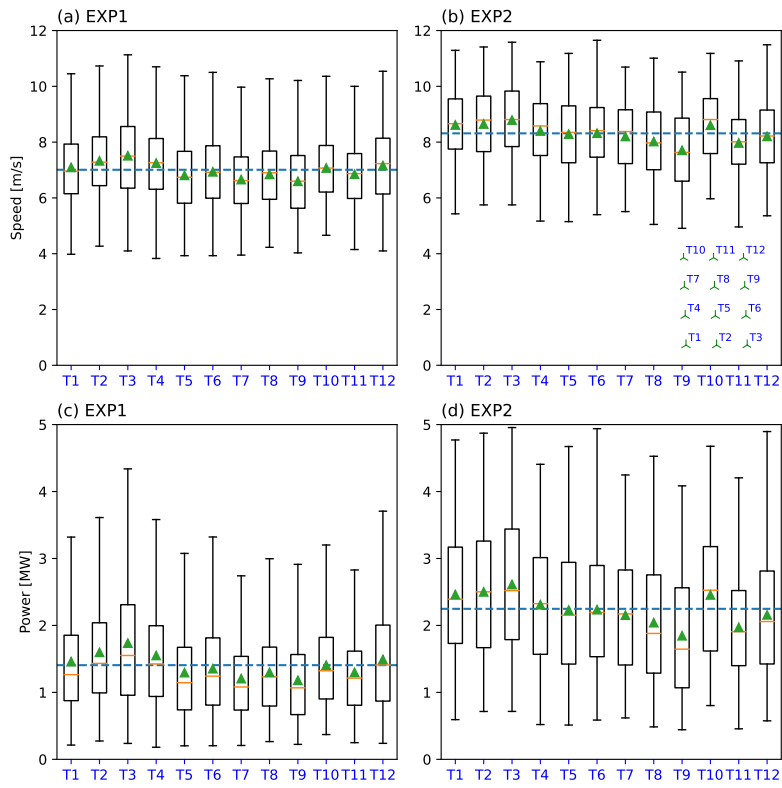
Figure 14. Box plots of 4 hours (from 08:00 to 12:00 UTC on September 24, 2016) for ambient wind speeds (a and b) and turbine powers (c and d) for the turbines in the Alpha Ventus wind farm. The average values (blue dashed lines) are 7 m/s and 8.3 m/s for (a) and (b), 1.4 MW and 2.25 MW for (c) and (d) respectively. The layout of the turbines in the Alpha Ventus wind farm is shown on the bottom right of panel (b).

5 Discussion

The turbulence in the wake behind a wind turbine primarily arises from shear due to reduced wind speed in the wake region
590 (Crespo et al., 1996; Quarton and Ainslie, 1990). In mesoscale modeling, incorporating turbulence kinetic energy (TKE) into wind farm parameterization is necessary due to the model's inability to resolve wakes at small scales (Fitch et al., 2012) . Fitch et al. (2012) assumes that a portion of the extracted energy from the mean wind becomes power (related to thrust coefficient C_T), while the remainder becomes TKE, proportional to $C_T - C_P$. Given WRF-SADLES's target resolution of a few dozen meters, where the wake is partially resolved, some added subgrid-scale TKE may be necessary. However, testing
595 Fitch's method in WRF-SADLES with subgrid-scale TKE using a TKE factor ($C_{TKE} = C_T - C_P$) revealed minimal influence on the far wake structure, except near the turbine. This raises questions about the validity of Fitch's assumption, as the TKE downstream should relate to wake deficit, which is linked to C_T, not $C_T - C_P$. In an idealized scenario where all TKE extracted

from the mean wind converts to power ($C_T = C_P$), according to Fitch, no TKE is generated, which is not appropriate. Thus, we imply that wind farm parameterization in mesoscale models should consider the relationship between added turbulence and

600   C_T, alongside factors like stability conditions.

The mesoscale-to-microscale downscaling method proposed by ~~Muñoz et al.~~ Muñoz-Esparza et al. (2014) and in (Bakhoday-Paskyabi et aimed to seamlessly transition atmospheric processes across scales. WRF-SADLES achieves this through nested simulations. However, in our case study (Fig. 11), WRF-LES simulations underestimated the strength of the low-level jet, with the vertical wind veer only half of the observed values. This underestimation occurred in both the WRF-LES domain (D04, 200-meter

605   resolution) and the WRF-SADLES domain (D04, 40-meter resolution).

We attribute this limitation to the resolution used in domain D04, which falls within the gray zone or 'terra incognita' for numerical models (Wyngaard, 2004). This zone represents a transition region between mesoscale and microscale, where traditional boundary layer parameterizations and LES are not accurately applicable. Here, turbulence activities may be misrepresented, leading to simulation inaccuracies. While WRF-SADLES simulations show some improvement, the small domain size likely

610   restricts its ability to fully correct the erroneous environmental conditions inherited from the inflow boundaries of D04. We attempted to bypass this issue by skipping the 200-meter resolution domain. However, this led to WRF model crashes, possibly due to the large grid ratio (1:25) not being supported.

6 Conclusion

In this paper, we present our implementation of a ~~simple actuator disc model for large eddy simulation~~ Simple Actuator Disc

615   model for Large Eddy Simulation (SADLES) within the Weather Research and Forecast ~~(WRF)model~~ model (WRF-SADLES). Unlike other previous implementations of wind turbine parameterization within WRF, such as the General Actuator Disc (GAD) (Mirocha et al., 2014; Kale et al., 2022), ~~SADLES~~ WRF-SADLES only requires the power curve and thrust coefficient curve—the same information used in wind farm parameterization (WFP Fitch et al., 2012) that is already included in WRF. The purpose of ~~SADLES~~ WRF-SADLES is to explicitly simulate the wakes of multiple wind farms in online nested downscaling

620   applications from realistic atmospheric conditions. The target resolution of the WRF-SADLES is ~~the~~ intermediate between the GAD model and the WFP, in which one turbine is represented by a few grid points.

~~SADLES uses~~ WRF-SADLES employs the traditional actuator disc model, ~~where the turbine is represented by~~ representing the turbine as a thin disc that ~~causes a thrustforce that slows down the~~ generates thrust, slowing down ambient wind speed. ~~A caveat of this method is the assumption of a uniform thrust coefficient for the actuator disc, and the lack of tangential~~

625   ~~velocity tendency and explicit turbulence behind the wind turbine, as demonstrated in our idealized experiment~~ In our idealized experiments with a single 5-MW turbine (Section 3). ~~However, the generated turbulence is still represented implicitly as the production of turbulent kinetic energy, which affects eddy diffusivity. When~~ , WRF-SADLES demonstrated good agreement compared to a dedicated LES model (the PALM model), ~~the simulated wake using~~ which incorporates rotation in its actuator disc model, providing a more comprehensive representation. Interestingly, at our target resolution of 30 meters, WRF-SADLES

630 ~~has better agreement between the 30-m and 10-m resolutions~~ exhibited better agreement with the 10-meter resolution than the PALM model.

We assessed two methods for evaluating the axial induction factor: direct evaluation (Option 1) using data points at and in front of the turbine, and inferred evaluation (Option 2) using 1D momentum theory. The results demonstrated strong agreement between the two methods. We recommend employing Option 2 due to its independence from model resolution and its ability to avoid potential issues associated with Option 1, as discussed in Section 2.1.

~~We also demonstrate the application of SADLES using a real-data simulation (Section 4) that downscales a realistic dataset~~ (Additionally, we experimented with adding subgrid-scale turbulence kinetic energy (TKE) at the actuator disc, similar to the approach by Fitch et al. (2012). However, the effect of added TKE only influenced a short distance from the turbine, and the far wake structures, including wake deficit and turbulent intensity, remained similar regardless of the presence of added TKE. Therefore, we recommend deactivating this option (i.e. $f_{TKE} = 0$) for practical application, partly because the rationale behind the method does not reflect reality.

We conducted a brief validation of WRF-SADLES using observational data from the FINO1 offshore meteorological mast station. This data included measurements from a cup anemometer at 90 meters height, as well as vertical and horizontal wind profiles obtained by LiDAR. The simulation downscales the ERA5 ~~data)~~ global reanalysis from a coarse resolution (~~about~~ approximately 31 ~~km~~ kilometers) to a turbine scale resolution (40 ~~m). The downscaling is performed using~~ meters). This downscaling is achieved through a system of five nested domains, with the outer three domains simulating mesoscale processes and the two inner domains simulating eddy turbulence. ~~In our specific experiment, we found little influence between the turbines within the Alpha Ventus wind farm, while the main influence is from the wind farm~~ The results demonstrate good agreement in the wake deficit observed at the FINO1 location between WRF-SADLES and the actual observations. However, there is a discrepancy in the timing of the wake deficit occurrence. We attribute this error not to the turbine model itself, but to the intermediate 200-meter resolution LES domain. This domain serves as the transitional zone between mesoscale and microscale, where turbulence activity is not accurately represented.

Finally, we present an example of farm-to-farm interaction at the Alpha Ventus wind farm near the FINO1 station. Here, the wind farm to the ~~southwest. The presence of this wind farm reduces the~~ southeast of Alpha Ventus leads to a reduction in ambient wind speed by ~~about 14%and the~~ approximately 16%, resulting in an average turbine power ~~by 35%~~ decrease of 38% during a 4-hour analysis window.

We ~~have published our code as open source to encourage further open research in the field of~~ 've made our code openly available to promote further research in wind energy. Our code distribution ~~also~~ includes our implementation of the cell perturbation method (Muñoz-Esparza et al., 2014), ~~which is essential for the~~ crucial for turbulence development in nested LES.

660 ~~It should be noted that SADLES is currently limited by the assumption of a disc always being perpendicular to the ambient flow, so wake deflection cannot currently be simulated. Some potential areas for further development of SADLES include the investigation of the TKE factor in wake representation and the inclusion of a parameterized net-tangential velocity tendency, which would enable the investigation of the~~ While WRF-SADLES demonstrates promising capabilities for meso-to-micro downscaling, addressing issues in the transition resolutions will be crucial for enhancing wake predictions. Future development

665 areas for WRF-SADLES could involve implementing yaw misalignment to enable wake deflection and investigating turbine yaw control . In this study, we validated the WRF-SADLES model against another LES model, but further comparisons with observational data are necessary to fully verify the model's accuracy. strategies.

Our WRF-SADLES initial released code with an example idealized settings for the 30-m simulation can be downloaded from: (?). A short WRF-SADLES user's guide can be obtained from WRF-SADLES's Github repository: . The WRF-ARW
670 model can be downloaded from: . The PALM model can be downloaded from: . The ERA5 hourly reanalysis can be download from: . The information of turbines can be downloaded from: (Larsén and Fischereit, 2021).

Appendix A: ~~Additonal~~ Additional WRF namelist options

Table A1. Summary of ~~SADLES~~ WRF-SADLES namelist options

Namelist options (`&physics`)	Default value	Description
`sadles_opt` (max_domains)	0	=0 turn off SADLES for the current domain; =1 or 2: use Option 1 (direct) or Option 2 (inferred) for the induction factor, respectively
`sadles_startmin` (max_domains)	0	Time to start SADLES in minutes
`sadles_maxradius` *	120	Max turbine radius in meter,
`sadles_mindx` *	20	Min Δx in meter,
`sadles_mindz` *	20	Min Δz in meter,
`sadles_tkefact`	0.5	f_{KTE}, from 0 to 1 (see the text for the description)
`ideal_f`	0.0001	Coriolis force (`em_les` only),
`ideal_znt`	-1.	Surface roughness length (`em_les` only, only effective for positive values).

* These values are used to allocate arrays within the SADLES module.

Table A2. Summary of cell perturbation namelist options

Namelist options (`&cpert`)	Default value	Description
`cell_pert_xs` (max_domains)	0	=1 will apply cell perturbation for the western boundary
`cell_pert_xe` (max_domains)	0	=1 will apply cell perturbation for the eastern boundary
`cell_pert_ys` (max_domains)	0	=1 will apply cell perturbation for the southern boundary
`cell_pert_ye` (max_domains)	0	=1 will apply cell perturbation for the northern boundary
`cell_pert_magnitude`	0.5	Magnitude of the cell perturbation
`cell_pert_interval` (max_domains) [*]	320	Interval to apply the perturbation in seconds
`cell_pert_k1`	8	Bottom level of the transition layer for cell perturbation
`cell_pert_k2`	16	Top level of the transition layer for cell perturbation

[*] The interval should be approximately $\frac{8\Delta x}{U}$, where U is the average wind speed during the simulation. For example, with $\Delta x = 200$ m and $U = 5$ m/s, the interval will be approximately $\frac{8(200\,\text{m})}{5\,\text{m/s}} = 320$ s.

Code and data availability.

Our WRF-SADLES initial release code with an example of idealized settings for the 30-meter simulation can be downloaded
675 from: https://doi.org/10.5281/zenodo.10803669 (Bui, 2023). A short WRF-SADLES user's guide can be obtained from WRF-SADLES's
GitHub repository: https://github.com/haibuihoang/WRF-SADLES. The WRF-ARW model can be downloaded from https://
github.com/wrf-model/WRF. The PALM model can be downloaded from https://gitlab.palm-model.org/releases/palm_model_
system. The ERA5 hourly reanalysis can be downloaded from: https://cds.climate.copernicus.eu/. The information of turbines
can be downloaded from: https://doi.org/10.5281/zenodo.4668613 (Larsén and Fischereit, 2021).

680 *Author contributions.* Hai Bui proposed and implemented the WRF-SADLES code, conducted the WRF-SADLES simulations, and wrote
the manuscript. Mostsafa provided turbine information, revised the manuscript, and assisted with several technical discussions. Moham-
madreza contributed by writing the description of the PALM model, performing the PALM simulation, and assisting with manuscript revi-
sions.

Competing interests.

685 All authors declare that they have no competing of interest.

Acknowledgements. The work is a part of the HIghly advanced Probabilistic design and Enhanced Reliability methods for high-value,
cost-efficient offshore WIND (HIPERWIND) project, which has received funding from the European Union's Horizon 2020 Research and
Innovation Programme under Grant Agreement No. 101006689. The simulations were performed on resources provided by project NN9871K
by UNINETT Sigma2 - the National Infrastructure for High Performance Computing and Data Storage in Norway.

References

Anderson, C.: Wind turbines: Theory and practice, Cambridge University Press, 2020.

Ardillon, E., Paskyabi, M. B., Cousin, A., Dimitrov, N., Dupoiron, M., Eldevik, S., Fekhari, E., Ferreira, C., Guiton, M., Jezequel, B., et al.: Turbine loading and wake model uncertainty, Deliverable D3.2 for HIPERWIND project, https://www.hiperwind.eu/, 2023.

Bakhoday-Paskyabi, M., Bui, H., and Mohammadpour Penchah, M.: Atmospheric-Wave Multi-Scale Flow Modelling, Deliverable D2.1 for HIPERWIND project, https://www.hiperwind.eu/, 2022a.

Bakhoday-Paskyabi, M., Krutova, M., Bui, H., and Ning, X.: Multiscale Simulation of Offshore Wind Variability During Frontal Passage: Brief Implication on Turbines' Wakes and Load, in: Journal of Physics: Conference Series, vol. 2362, p. 012003, IOP Publishing, 2022b.

Baldauf, M., Seifert, A., Förstner, J., Majewski, D., Raschendorfer, M., and Reinhardt, T.: Operational convective-scale numerical weather prediction with the COSMO model: Description and sensitivities, Monthly Weather Review, 139, 3887–3905, 2011.

Breton, S.-P., Sumner, J., Sørensen, J. N., Hansen, K. S., Sarmast, S., and Ivanell, S.: A survey of modelling methods for high-fidelity wind farm simulations using large eddy simulation, Philosophical Transactions of the Royal Society A: Mathematical, Physical and Engineering Sciences, 375, 20160 097, 2017.

Bui, H.: Simple Actuator Disc for Large Eddy Simulation (SADLES), https://doi.org/10.5281/zenodo.10803669, 2023.

Bui, H. and Bakhoday-Paskyabi, M.: Mesoscale Simulation of Open Cellular Convection: Roles of Model Resolutions and Physics Parameterizations, in: Journal of Physics: Conference Series, vol. 2362, p. 012006, IOP Publishing, 2022.

Burton, T., Jenkins, N., Sharpe, D., and Bossanyi, E.: Wind energy handbook, John Wiley & Sons, 2011.

Calaf, M., Meneveau, C., and Meyers, J.: Large eddy simulation study of fully developed wind-turbine array boundary layers, Physics of fluids, 22, 015 110, 2010.

Churchfield, M., Wang, Q., Scholbrock, A., Herges, T., Mikkelsen, T., and Sjöholm, M.: Using high-fidelity computational fluid dynamics to help design a wind turbine wake measurement experiment, in: Journal of Physics: Conference Series, vol. 753, p. 032009, IOP Publishing, 2016.

Crespo, A., Herna, J., et al.: Turbulence characteristics in wind-turbine wakes, Journal of wind engineering and industrial aerodynamics, 61, 71–85, 1996.

Deardorff, J. W.: Stratocumulus-capped mixed layers derived from a three-dimensional model, Boundary-layer meteorology, 18, 495–527, 1980.

Fischereit, J., Brown, R., Larsén, X. G., Badger, J., and Hawkes, G.: Review of Mesoscale Wind-Farm Parametrizations and Their Applications, Boundary-Layer Meteorology, 182, 175–224, 2022.

Fitch, A. C., Olson, J. B., Lundquist, J. K., Dudhia, J., Gupta, A. K., Michalakes, J., and Barstad, I.: Local and mesoscale impacts of wind farms as parameterized in a mesoscale NWP model, Monthly Weather Review, 140, 3017–3038, 2012.

Fleming, P. A., Gebraad, P. M., Lee, S., van Wingerden, J.-W., Johnson, K., Churchfield, M., Michalakes, J., Spalart, P., and Moriarty, P.: Evaluating techniques for redirecting turbine wakes using SOWFA, Renewable Energy, 70, 211–218, 2014.

Gaertner, E., Rinker, J., Sethuraman, L., Zahle, F., Anderson, B., Barter, G. E., Abbas, N. J., Meng, F., Bortolotti, P., Skrzypinski, W., et al.: IEA wind TCP task 37: definition of the IEA 15-megawatt offshore reference wind turbine, Tech. rep., National Renewable Energy Lab.(NREL), Golden, CO (United States), 2020.

Göçmen, T., Van der Laan, P., Réthoré, P.-E., Diaz, A. P., Larsen, G. C., and Ott, S.: Wind turbine wake models developed at the technical university of Denmark: A review, Renewable and Sustainable Energy Reviews, 60, 752–769, 2016.

690

695

700

705

710

715

720

725

Hersbach, H., Bell, B., Berrisford, P., Hirahara, S., Horányi, A., Muñoz-Sabater, J., Nicolas, J., Peubey, C., Radu, R., Schepers, D., et al.: The ERA5 global reanalysis, Quarterly Journal of the Royal Meteorological Society, 146, 1999–2049, 2020.

Hong, S.-Y., Noh, Y., and Dudhia, J.: A new vertical diffusion package with an explicit treatment of entrainment processes, Mon. Weather Rev., 134, 2318–2341, 2006.

Iacono, M. J., Delamere, J. S., Mlawer, E. J., Shephard, M. W., Clough, S. A., and Collins, W. D.: Radiative forcing by long-lived greenhouse gases: Calculations with the AER radiative transfer models, J. Geophys. Res. Atmos., 113, 2008.

Jiménez, P. A., Dudhia, J., González-Rouco, J. F., Navarro, J., Montávez, J. P., and García-Bustamante, E.: A revised scheme for the WRF surface layer formulation, Monthly weather review, 140, 898–918, 2012.

Jonkman, J., Butterfield, S., Musial, W., and Scott, G.: Definition of a 5-MW reference wind turbine for offshore system development, Tech. rep., National Renewable Energy Lab.(NREL), Golden, CO (United States), 2009.

Kale, B., Buckingham, S., van Beeck, J., and Cuerva-Tejero, A.: Implementation of a generalized actuator disk model into WRF v4. 3: A validation study for a real-scale wind turbine, Renewable Energy, 197, 810–827, 2022.

Kumer, V.-M., Reuder, J., and Furevik, B. R.: A comparison of LiDAR and radiosonde wind measurements, Energy Procedia, 53, 214–220, 2014.

Larsén, X. G. and Fischereit, J.: A case study of wind farm effects using two wake parameterizations in WRF (V3.7.1) in the presence of low level jets, https://doi.org/10.5281/zenodo.4668613, 2021.

Lee, J. C. and Lundquist, J. K.: Evaluation of the wind farm parameterization in the Weather Research and Forecasting model (version 3.8. 1) with meteorological and turbine power data, Geoscientific Model Development, 10, 4229–4244, 2017.

Lilly, D. K.: The representation of small-scale turbulence in numerical simulation experiments, IBM Form, pp. 195–210, 1967.

Lin, D., Khan, B., Katurji, M., Bird, L., Faria, R., and Revell, L. E.: WRF4PALM v1. 0: a mesoscale dynamical driver for the microscale PALM model system 6.0, Geoscientific Model Development, 14, 2503–2524, 2021.

Maronga, B., Gryschka, M., Heinze, R., Hoffmann, F., Kanani-Sühring, F., Keck, M., Ketelsen, K., Letzel, M. O., Sühring, M., and Raasch, S.: The Parallelized Large-Eddy Simulation Model (PALM) version 4.0 for atmospheric and oceanic flows: model formulation, recent developments, and future perspectives, Geoscientific Model Development, 8, 2515–2551, 2015.

Maronga, B., Banzhaf, S., Burmeister, C., Esch, T., Forkel, R., Fröhlich, D., Fuka, V., Gehrke, K. F., Geletič, J., Giersch, S., et al.: Overview of the PALM model system 6.0, Geoscientific Model Development, 13, 1335–1372, 2020.

Mirocha, J., Kosovic, B., Aitken, M., and Lundquist, J.: Implementation of a generalized actuator disk wind turbine model into the weather research and forecasting model for large-eddy simulation applications, Journal of Renewable and Sustainable Energy, 6, 013 104, 2014.

Moeng, C.-H. and Wyngaard, J. C.: Spectral analysis of large-eddy simulations of the convective boundary layer, Journal of Atmospheric Sciences, 45, 3573–3587, 1988.

Mukul Tewari, N., Tewari, M., Chen, F., Wang, W., Dudhia, J., LeMone, M., Mitchell, K., Ek, M., Gayno, G., Wegiel, J., et al.: Implementation and verification of the unified NOAH land surface model in the WRF model (Formerly Paper Number 17.5), in: Proceedings of the 20th Conference on Weather Analysis and Forecasting/16th Conference on Numerical Weather Prediction, Seattle, WA, USA, vol. 14, 2004.

Muñoz-Esparza, D., Kosović, B., Mirocha, J., and van Beeck, J.: Bridging the transition from mesoscale to microscale turbulence in numerical weather prediction models, Boundary-layer meteorology, 153, 409–440, 2014.

Muñoz-Esparza, D., Kosović, B., Van Beeck, J., and Mirocha, J.: A stochastic perturbation method to generate inflow turbulence in large-eddy simulation models: Application to neutrally stratified atmospheric boundary layers, Phys. Fluids, 27, 035 102, 2015.

Ning, X., Paskyabi, M. B., Bui, H. H., and Penchah, M. M.: Evaluation of sea surface roughness parameterization in meso-to-micro scale simulation of the offshore wind field, Journal of Wind Engineering and Industrial Aerodynamics, 242, 105 592, 2023.

Onel, H. C. and Tuncer, I. H.: Short-Term Numerical Forecasting of Near-Ground Wind Fields Using OpenFOAM Coupled With WRF, in: AIAA SCITECH 2023 Forum, p. 1737, 2023.

Porté-Agel, F., Bastankhah, M., and Shamsoddin, S.: Wind-turbine and wind-farm flows: A review, Boundary-layer meteorology, 174, 1–59, 2020.

Pryor, S. C., Shepherd, T. J., Volker, P. J., Hahmann, A. N., and Barthelmie, R. J.: "Wind Theft" from onshore wind turbine arrays: sensitivity to wind farm parameterization and resolution, Journal of Applied Meteorology and Climatology, 59, 153–174, 2020.

Quarton, D. and Ainslie, J.: Turbulence in wind turbine wakes, Wind Engineering, pp. 15–23, 1990.

Saiki, E. M., Moeng, C.-H., and Sullivan, P. P.: Large-eddy simulation of the stably stratified planetary boundary layer, Boundary-Layer Meteorology, 95, 1–30, 2000.

Salim, M. H., Schlünzen, K. H., Grawe, D., Boettcher, M., Gierisch, A. M., and Fock, B. H.: The microscale obstacle-resolving meteorological model MITRAS v2. 0: model theory, Geoscientific Model Development, 11, 3427–3445, 2018.

Skamarock, W. C., Klemp, J. B., Dudhia, J., Gill, D. O., Liu, Z., Berner, J., Wang, W., Powers, J. G., Duda, M. G., Barker, D. M., et al.: A description of the advanced research WRF model version 4, National Center for Atmospheric Research: Boulder, CO, USA, 145, 145, 2019.

Thompson, G., Field, P. R., Rasmussen, R. M., and Hall, W. D.: Explicit forecasts of winter precipitation using an improved bulk microphysics scheme. Part II: Implementation of a new snow parameterization, Mon. Weather Rev., 136, 5095–5115, 2008.

Volker, P., Badger, J., Hahmann, A. N., and Ott, S.: The Explicit Wake Parametrisation V1. 0: a wind farm parametrisation in the mesoscale model WRF, Geoscientific Model Development, 8, 3715–3731, 2015.

Vollmer, L., van Dooren, M., Trabucchi, D., Schneemann, J., Steinfeld, G., Witha, B., Trujillo, J., and Kühn, M.: First comparison of LES of an offshore wind turbine wake with dual-Doppler lidar measurements in a German offshore wind farm, in: Journal of Physics: Conference Series, vol. 625, p. 012001, IOP Publishing, 2015.

Wang, Q., Luo, K., Yuan, R., Wang, S., Fan, J., and Cen, K.: A multiscale numerical framework coupled with control strategies for simulating a wind farm in complex terrain, Energy, 203, 117 913, 2020.

Witha, B., Steinfeld, G., and Heinemann, D.: High-resolution offshore wake simulations with the LES model PALM, in: Wind energy-impact of turbulence, pp. 175–181, Springer, 2014.

Wyngaard, J. C.: Toward numerical modeling in the "Terra Incognita", Journal of the atmospheric sciences, 61, 1816–1826, 2004.

Zhang, C., Wang, Y., and Hamilton, K.: Improved representation of boundary layer clouds over the southeast Pacific in ARW-WRF using a modified Tiedtke cumulus parameterization scheme, Mon. Weather Rev., 139, 3489–3513, 2011.